Satellites reveal Earth's seasonally shifting dust emission sources

Adrian Chappell, Nicholas P Webb, Mark Hennen, Kerstin Schepanski, Philippe Ciais, Yves Balkanski, Charles S Zender, Ina Tegen, Zhenzhong Zeng, Daniel Tong, et al.

Satellites reveal Earth's seasonally shifting dust emission sources

Adrian Chappell, Nicholas P Webb, Mark Hennen, Kerstin Schepanski, Philippe Ciais, Yves Balkanski, Charles S Zender, Ina Tegen, Zhenzhong Zeng, Daniel Tong, et al.

Satellites reveal Earth's seasonally shifting dust emission sources

Adrian Chappell, Nicholas P. Webb, Mark Hennen, Kerstin Schepanski, Philippe Ciais, Yves Balkanski, Charles S. Zender, Ina Tegen, Zhenzhong Zeng, Daniel Tong, Barry Baker, Marie Ekström, Matt Baddock, Frank D. Eckardt, Tarek Kandakji, Jeffrey A. Lee, Mohamad Nobakht, Johanna von Holdt, John F. Leys

PII: S0048-9697(23)02071-5

DOI: https://doi.org/10.1016/j.scitotenv.2023.163452

Reference: STOTEN 163452

To appear in: *Science of the Total Environment*

Received date: 14 February 2023

Revised date: 31 March 2023

Accepted date: 7 April 2023

Please cite this article as: A. Chappell, N.P. Webb, M. Hennen, et al., Satellites reveal Earth's seasonally shifting dust emission sources, *Science of the Total Environment* (2023), https://doi.org/10.1016/j.scitotenv.2023.163452

Satellites reveal Earth's seasonally shifting dust emission sources

Adrian Chappell[1]*, Nicholas P. Webb[2], Mark Hennen[1], Kerstin Schepanski[3], Philippe Ciais[4,5], Yves Balkanski[4], Charles S. Zender[6], Ina Tegen[7], Zhenzhong Zeng[8], Daniel Tong[9], Barry Baker[9], Marie Ekström[1], Matt Baddock[10], Frank D. Eckardt[11], Tarek Kandakji[12], Jeffrey A. Lee[13], Mohamad Nobakht[14], Johanna von Holdt[11], John F. Leys[15,16].

[1]School of Earth and Environmental Science, Cardiff University, Cardiff, UK.
[2]USDA-ARS Jornada Experimental Range, Las Cruces, New Mexico, USA.
[3]Institute of Meteorology, Freie Universität Berlin, Germany.
[4]Laboratoire des Sciences du Climat eipcct de l'Environnement, CEA CNRS UPSACLAY, Gif-sur-Yvette, France.
[5]Climate and Atmosphere Research Center (CARE-C), The Cyprus Institute, 20 Konstantinou Kavafi Street, 2121 Nicosia, Cyprus.
[6]Department of Earth System Science, University of California, Irvine, USA.
[7]Leibniz Institute for Tropospheric Research, Leipzig, Germany.
[8]School of Environmental Science and Engineering, Southern University of Science and Technology, Shenzhen 518055, China
[9]Department of Atmospheric, Oceanic and Earth Sciences, George Mason University, Fairfax, VA 22030 USA.
[10]Geography and Environment, Loughborough University, Loughborough, UK.
[11]Department of Environmental and Geographical Science, University of Cape Town, Rondebosch 7701, South Africa.
[12]Centre for Earth Observation, Yale University, USA.
[13]Texas Tech University, Texas, USA
[14]Telespazio UK Ltd, Capability Green, Luton LU1 3LU, Bedfordshire, UK.
[15] Science Division, Department of Planning, Industry and Environment, Gunnedah, Australia.
[16] Fenner School of Environment and Society, Australian National University, Canberra, Australia.

*Correspondence to: chappella2@cardiff.ac.uk

Abstract

Establishing mineral dust impacts on Earth's systems requires numerical models of the dust cycle. Differences between dust optical depth (DOD) measurements and modelling the cycle of dust emission, atmospheric transport, and deposition of dust indicate large model uncertainty due partially to unrealistic model assumptions about dust emission frequency. Calibrating dust cycle models to DOD measurements typically in North Africa, are routinely used to reduce dust model magnitude. This calibration forces modelled dust emissions to match atmospheric DOD but may hide the correct magnitude and frequency of dust emission events at source, compensating biases in other modelled processes of the dust cycle. Therefore, it is essential to improve physically based dust emission modules.

Here we use a global collation of satellite observations from previous studies of dust emission point source (DPS) dichotomous frequency data. We show that these DPS data have little-to-no relation with MODIS DOD frequency. We calibrate the albedo-based dust emission model using the frequency distribution of those DPS data. The global dust emission uncertainty constrained by DPS data (±3.8 kg m^{-2} y^{-1}) provides a benchmark for dust emission model development. Our calibrated model results reveal much less global dust emission (29.1±14.9 Tg y^{-1}) than previous estimates, and show seasonally shifting dust emission predominance within and between hemispheres, as opposed to a persistent North African dust emission primacy widely interpreted from DOD measurements.

Earth's largest dust emissions, proceed seasonally from East Asian deserts in boreal spring, to Middle Eastern and North African deserts in boreal summer and then Australian shrublands in boreal autumn-winter. This new analysis of dust emissions, from global sources of varying geochemical properties, have far-reaching implications for current and future dust-climate effects. For more reliable coupled representation of dust-climate projections, our

findings suggest the need to re-evaluate dust cycle modelling and benefit from the albedo-based parameterisation.

1. Introduction

In Earth's systems mineral dust plays a vital role (Shao et al. 2011) impacting climate, air quality and human health (Favet et al. 2013; Kok et al. 2023; Tong et al. 2017), and influencing dryland ecosystem services (Peters et al. 2015) driven by changing soil erosion and desertification (Rodriguez-Caballero et al. 2022). Factors controlling aeolian sediment transport, underpinning dust emission, are variable over space and time. Consequently, dust impact studies rely on numerical models that simulate the cycle of emission, atmospheric transport, and deposition of dust (Mahowald et al. 2010) (called dust models or aerosol transport models but for clarity, hereafter dust cycle models; (Shao et al. 2011)). Amassed observations from the last two decades including dust optical depth (DOD) measurements show that large amounts of atmospheric dust reside persistently and predominantly over major dust sources of North Africa and the Middle East (Engelstaedter et al. 2006; Ginoux et al. 2012; Prospero et al. 2002; Tegen et al. 2002; Woodward 2001). However, comparing dust cycle models with DOD also indicate large errors in simulated dust magnitude and geochemical properties (Evan et al. 2014; Huneeus et al. 2011; Kok et al. 2023). Consequently, dust cycle models are calibrated to DOD and often to a particular region which is typically North Africa (Huneeus et al. 2011). However, DOD is not directly related to dust emission magnitude and frequency which are inextricably bound together in the underpinning sediment transport equation (Lee and Tchakerian 1995; Wolman and Miller 1960). Assuming globally consistent calibration, this forces global dust emissions to match North African dust suspended in the atmosphere. As the observed dust plumes are at often unknown distances from dust sources, the correct magnitude and frequency and geographical distribution of

emissions from sources are hidden. This calibration approach is implicated in long-standing, hidden weaknesses (Zender et al. 2003a) (*Chappell et al., under review JGR-Atmos*.) in classical dust emission models and may also hide errors in boundary data sets (Zender et al. 2003b). We do not dispute the utility and benefits of DOD measurements to calibrate dust cycle models , we propose in this study a first phase in which the dust emission model is constrained by dust emission observations.

Our focus here is to establish at-source dust emission magnitude and frequency to calibrate dust emission modelling. By separating the calibration of dust emission modelling from the calibration of dust cycle modelling to dust aerosol loading, our approach provides new insights of dust emission magnitude and frequency and offers opportunities to improve dust cycle modelling and dust-climate impacts. We first describe the albedo-based sediment transport equation and the frequency of dust emission events poorly constrained by unrealistic assumptions of grain-scale threshold, static over time and fixed over space, and of an infinite supply of loose, erodible material everywhere across the Earth's land surface. A description of long-established satellite observed dust emission point source (DPS) data is then provided to compare with the well-known DOD data. The albedo-based dust emission model is described. We then show how the poorly constrained dust emission frequency distribution, common to classical dust emission modelling, can be improved by using the dust emission frequency distribution of DPS data. A dust emission model calibration is formed and then validated to establish dust emission model uncertainty. A data section is provided to demonstrate how the modelling is implemented and regions and land covers are also defined for the calculation of statistical summaries. A standard results presentation is enhanced with data layers animated using video (Appendix 2) to illustrate the fundamental differences between the albedo-based dust emission model calibrated using DPS frequency data and DOD frequency data. The Discussion explains why the results from this approach diverge

radically whilst complementing previous work and how our results are entirely consistent with well-known regional dust climatologies and large dust concentrations above North African and Middle eastern regions. Finally, we consider the implications of our results for future dust-climate studies.

2. Methods and data

2.1 Albedo-based sediment transport for dust emission modelling (AEM)

We calculated albedo-based sediment transport following the established approach (Chappell and Webb 2016; Hennen et al. 2022; Hennen et al. 2023) using the modified saltation flux Q (g m^{-1} s^{-1}) as

$$Q_{AEM} = c\frac{\rho_a}{g}u_{s*}^3(\omega)\left(1+\frac{u_{*ts}(d)H(w)}{u_{s*}(\omega)}\right)\left(1-\left(\frac{u_{*ts}(d)H(w)}{u_{s*}(\omega)}\right)^2\right)\begin{cases}u_{s*}(\omega) > u_{*ts}(d)H(w)\\ 0\end{cases}. \quad \text{(Eq.1)}$$

The air density ρ_a is fixed for simplicity at 1.23 kg m^{-3} and gravitational acceleration g is 9.81 m s^{-2}. The scaling parameter is c=1 (Darmenova et al. 2009). Notably, this formulation does not use the above canopy wind friction velocity u_* of classical sediment transport equations (Namikas and Sherman 1997). Instead a direct estimate of the soil surface wind friction velocity (u_{s*}; m s^{-1}) is provided using albedo (ω) which is influenced by all scales of soil surface roughness (explained below). An example of the spatial distribution of u_{s*} is shown below in this section and the need for the latter in the sediment transport equation is explained in detail elsewhere (Webb et al. 2020).

The u_{*ts} of a given particle size with diameter d (μm) is the entrainment threshold of a dry, smooth surface which the u_{s*} must exceed to trigger sediment transport and dust emission. We used the u_{*ts} formulation common to many dust emission models described elsewhere (Marticorena and Bergametti 1995) and included in our Appendix 1. The grain scale u_{*ts} is fixed over space for a given substrate (typically soil) type and is also static over

time. The u_{*ts} is adjusted by the function H (Eq. 1) which depends on the gravimetric topsoil moisture w (m^3 m^{-3}) which itself depends on clay content (Fécan et al. 1999). This parameterization $H(w)$ is commonly applied in dust emission modelling, is outlined in our Appendix 1, and described in detail elsewhere (Bergametti et al. 2016; Xi and Sokolik 2015). Hereafter and for brevity, we remove the dependencies in the terms used.

The key to unlocking our albedo-based approach is the direct estimation of u_{s*} normalised by wind speed U at height h (U_h) by relating the shadow of land surface roughness to its shelter (Raupach 1992). Established work (Chappell et al. 2010; Chappell and Webb 2016; Chappell et al. 2018; Ziegler et al. 2020) provides a robust direct empirical estimate of u_{s*}/U_h with an estimation uncertainty of 0.027 m s^{-1}

$$\frac{u_{s*}}{U_h} = 0.0311\left(exp\frac{-\omega_{ns}{}^{1.131}}{0.016}\right) + 0.007. \quad \text{(Eq. 2)}$$

The ω_{ns} is rescaled normalised shadow (ω_n) from a MODIS range ($\omega_{n\,min}$=0, $\omega_{n\,max}$=35) at nadir ($\theta = 0°$), to the range of the calibrated data (a=0.0001 to b=0.1) (Chappell and Webb 2016) as:

$$\omega_{ns} = \frac{(a-b)(\omega_n(\theta)-\omega_n(\theta)_{max})}{(\omega_n(\theta)_{min}-\omega_n(\theta)_{max})} + b. \quad \text{(Eq. 3)}$$

The complement of albedo is shadow $1 - \omega_{dir}(0°,\ \lambda)$ and retains spectral (λ) information e.g., soil moisture, organic carbon and minerology. We remove the spectral information by dividing the shadow by the reflectance when viewed and illuminated at nadir $\rho(0°,\ \lambda)$(Chappell et al. 2018):

$$\omega_n = \frac{1-\omega_{dir}(0°,\ \lambda)}{\rho(0°,\ \lambda)} = \frac{1-\omega_{dir}(0°)}{\rho(0°)}. \quad \text{(Eq. 4)}$$

We have demonstrated that any source of albedo and directional reflectance can be used and the results are scale invariant (Ziegler et al. 2020). Here, the normalization was implemented

using MODIS daily black sky albedo (500 m; MCD43A3 v6) to estimate ω_n. Spectral influences are here removed by dividing shadow by the MODIS isotropic parameter f_{iso}:

$$\omega_n(0°) = \frac{1-\omega_{dir}(0°,\lambda)}{f_{iso}(\lambda)} = \frac{1-\omega_{dir}(0°)}{f_{iso}}. \quad \text{(Eq. 5)}$$

Theoretically, this approach causes information on the land surface structure to be waveband independent (Chappell et al. 2007; Jacquemoud et al. 1992). The MODIS Nadir BRDF-Adjusted Reflectance (NBAR) is similarly capable of removing the spectral information across wavebands (Chappell et al. 2018).

2.2 Satellite-observed dust emission point sources (DPS) and dust optical depth (DOD)

Commonly, dust optical depth (DOD) from ground-based (AERONET) or satellite-based data are used to evaluate the performance and / or calibrate dust model simulations, including in Earth System Models (ESMs). Of the many AERONET stations available, only few are relevant for dust emission studies, being located at best on the margins of dust source areas. Their geographical location and information about atmospheric dust concentration causes AERONET station data to be difficult to relate to, and inconsistent with the validation of, satellite observed dust emission point source (DPS) or dust emission model results. On the other hand, DOD estimates from satellite observation are globally available across dust source regions (Ginoux et al., 2012). However, DOD is a total column measure (Dubovik et al. 2000) which does not enable a distinction between freshly emitted dust plumes and aged dust in the atmosphere. Furthermore, emitted dust particles tend to accumulate and remain trapped in topographic basins (Ginoux et al. 2012; Schepanski 2018; Schepanski et al. 2012). Consequently, DOD frequency of occurrence is not expected to be entirely consistent with DPS frequency of occurrence or dust emission model results. The DOD is only partially related to dust emission because atmospheric dust concentration is controlled by dust

emission magnitude and frequency (evident from Eq. 1), but also by the residence time of dust near the surface which depends on wind speed, and by dust deposition in the dust source region, a size dependent process. Furthermore, DOD (Deep Blue product) is well known to be largely restricted to bright land surfaces in the visible wavebands with reduced performance over areas where vegetation is present (cf., (Ginoux et al. 2012) end paragraph 46). Many of the limitations associated with DPS are similarly applicable to DOD. Specifically, DOD is unable to detect optically thin dust and is therefore similar to DPS with a high bias towards large amounts of dust in the atmosphere. We note the previously established strong spatial correlation R^2=0.85 between DOD and aerosol optical depth (Ginoux et al. 2012) which justifies the use here of our comparison with DOD. To calculate DOD, we used wavebands available from monthly Moderate Resolution Imaging Spectroradiometer (MODIS; MOD08 M3 V6.1 Deep Blue L2 Aerosol Product) at a 1° pixel resolution (Platnick 2015). We followed the same established approach (Ginoux et al. 2012) and set DOD>0.2 as the frequency of occurrence. The DOD was retrieved from those pixels in which dust emission was observed from DPS in space and time throughout 2001-2016.

We extend our north American calibration and validation work (Hennen et al. 2022; Hennen et al. 2023) using a global collation of existing studies of satellite observed dust emission point sources (DPS) (**Figure 1a**; **Table 1**). These studies provide the frequency of occurrence of dust emission sources based on visible dust plume events. Our global collation of DPS observations had 90,928 dust occurrences over different durations of their entire observation period (2001-2016) using MODIS and SEVIRI satellite sensors (Table 1) standardised to 1° grid boxes (**Figure 1a**). We establish the frequency of dust emission events using dichotomous DPS in comparison with dust optical depth (DOD>0.2) frequency of occurrence (Ginoux et al. 2012) (**Figure 1b**). Note that we are showing the DOD frequency only where DPS is known from observations to occur (**Figure 1b**).

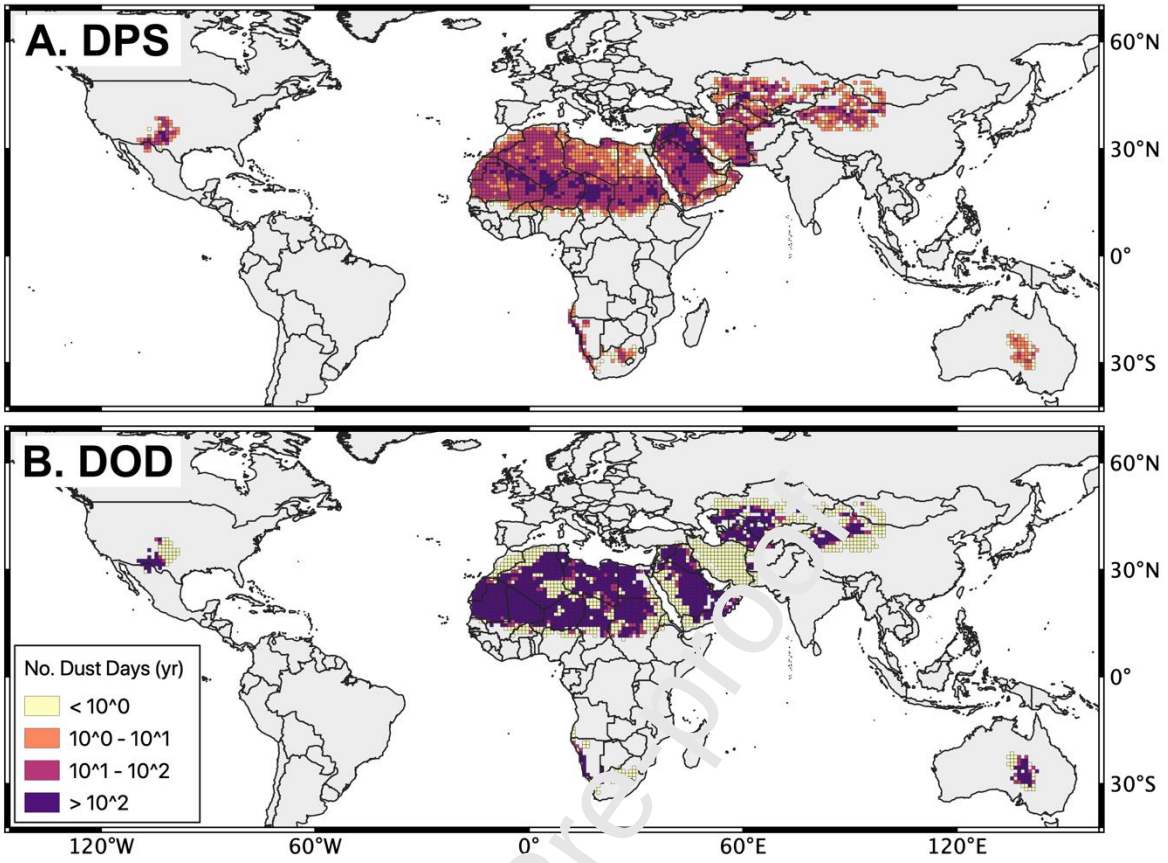

Figure 1. Satellite observed (MODIS and SEVIRI) dust emission point source (DPS) dichotomous frequency of occurrence data standardised to 1-degree grid boxes from several studies (**A**; details in **Table 1**) and restricting (**B**) the frequency of occurrence of MODIS (Deep Blue L2 Aerosol Product) DOD>0.2 (Ginoux et al. 2012) to the same grid boxes and time period (2001-2016).

Table 1. The major regions of dust sources, the sensors used and statistics to summarise the satellite observed dust emission point sources (DPS), including the mean wind friction velocity of the soil surface u_{s*} and the clay content (Hengl et al. 2017) used in the albedo-based model (AEM).

Region and source	**Sensor**	**Years**	**Total**	**Dust**	**Dust**	**Mean**	**Mean**

			days	**points**	**events**	**AEM u_{s*} (m s^{-1})**	**clay content (%)**
North Africa (Schepanski et al. 2007)	SEVIRI	2006-2010	1825	927	36490	0.26	10.04
Middle East (Hennen et al. 2019)	SEVIRI	2006-2013	2921	431	16781	0.28	14.06
Central Asia (Nobakht et al. 2021)	MODIS	2003-2012	3652	298	5201	0.27	18.69
Southern Africa (von Holdt et al. 2017)	MODIS	2005-2015	4016	36	697	0.26	16.27
North America (Lee et al. 2012)	MODIS	2001-2008	3286	13	69	0.36	19.99
Australia (Baddock et al. 2009; Bullard et al. 2008)	MODIS	2003-2006	1460	54	148	0.32	18.28
North America (Baddock et al. 2011)	MODIS	2001-2009	3286	12	56	0.33	19.67
Southern Africa (Eckardt et al. 2020)	SEVIRI	2006-2016	4017	26	135	0.25	18.43
North America (Kandakji et al.	MODIS	2001-2016	5843	48	189	0.35	19.82

2020)							

These studies use DPS data acquired from two space-borne sensors with contrasting orbits to produce multi-year, regional climatologies of dust emission sources. Details are provided in a companion manuscript (*Hennen et al., under review RSE; Supplementary manuscript supplied*). In brief, DPS data are produced either from i) MODIS (Terra and Aqua when possible) satellite data at a daily frequency and up to 250 m spatial resolution from a sun-synchronous low-Earth orbit, and ii) Spinning Enhanced Visible and Infrared Imager (SEVIRI) data at 15-minute frequency and up to 3 km resolution (nadir) from a geostationary orbit covering Europe and Africa. Each platform carries multispectral capability from visible to thermal infrared (TIR) wavebands (SEVIRI: 0.5 – 14.4mm / MODIS: 0.4 – 14.4mm) (**Table 1**).

For each method, absorption in the TIR by water vapour presents a potential limitation, reducing the cooling trend normally presented by atmospheric dust (Brindley et al., 2012). The presence of clouds or dust and/or smoke plumes from sources upwind may also prevent observation of the source of emission in a single image. The 15-minute frequency of SEVIRI data allow the observer to 'back-track' plume evolution through sequential images to the point of first observation, reducing the impact of overlapping plumes (Hennen et al. 2019). For MODIS imagery, the 250 m spatial resolution provides finer detail but smaller temporal revisit, allowing the observer to better detect individual plume shapes, partially mitigating overlapping plumes (Baddock et al. 2009). Varying surface TIR emissivity occurs due to spatial changes in surface condition (vegetation, geology), creating variations in the BTD profiles and altering the RGB renderings (Banks and Brindley 2013; Banks et al. 2019; Banks et al. 2018). During each of these limitation scenarios, subjective

interpretation improves upon non-dynamic automated retrieval algorithms, which are required to work in all surface and atmospheric conditions (Schepanski et al. 2012).

The shape recognition and decision-making abilities of DPS observed by humans currently exceeds those of automated approaches. Although human observations alleviate many of the limitations and prevent false positive observations (Lee et al. 2012) they are not without caveats (Sinclair and LeGrand 2019). Those recent caveats refer to the precise location of the DPS which are avoided using our grid box aggregations (see below). Typically, DPS studies establish and adhere to specific criteria for legitimate observation, including: i) observation must take place during an emission event, where the deflation surface is clearly identifiable at the head of emission plume; ii) the distinct dust source must not be obscured by either clouds or upwind dust/smoke overlapping emission plumes (Lee et al. 2012). Consequently, these data represent the cutting-edge of dust emission event observations, allowing spatial verification on the basis of individual events occurrence. The DPS is identified by a presence in dust emission, but the absence of dust emission is not recorded (dichotomous).

To make these DPS studies comparable, we reduced the resolution of the satellite observed dust emission point source observation coordinates to 1° consistent with the coarsest resolution (Schepanski et al. 2007). Table 1 enables the regional results to be described as a probability compared to the number of dust emission opportunities (number of DPS locations multiplied by the number of days in the study minus the number of missing coincident albedo data – *Hennen et al., under review RSE; Supplementary manuscript supplied*). Missing albedo data are caused by satellite remote sensing issues including cloud cover, sensor irregularities and coverage particularly across north Africa. Across all 9 studies a total of 37,352 unique DPS locations (Table 1) were aggregated into 1,945 unique 1° grid boxes, from which a total of 59,688 dust emissions were identified. Missing data ranged from

18.9% (North Africa) to 54.5% (Central Asia), with an average of 34.4% across all nine regions. Corresponding missing data were removed from both modelled and observed data to maintain consistency in results. For each of the DPS regions, we included mean values of the soil surface wind friction velocity (u_{s*}) and the clay content to illustrate the differences between dust source regions (Table 1).

2.3 Albedo-based dust emission model and calibration using dust emission point sources

From our standardised DPS dataset the probability of occurrence $P(DPS > 0)$ was calculated to approximate the probability of sediment transport $P(Q > 0)$ and dust (F) emission $P(F > 0)$ at those DPS locations and study durations, equal in the albedo-based dust emission model (AEM) to the frequency u_{s*} exceeds the entrainment threshold (u_{*ts}) adjusted only by the soil moisture function (H):

$$P(DPS > 0) \approx P(Q > 0) \propto P(F > 0) = u_{s*} > u_{*ts}H \begin{cases} 1 \\ 0, \end{cases} \quad \text{(Eq. 6)}$$

The correct magnitude and frequency of the AEM depends on the correct $P(F > 0)$, which itself depends on the correct $u_{*ts}H$. However, long-standing dust emission schemes (Marticorena and Bergametti 1995; Shao et al. 1996) assume a smooth soil surface covered by an infinite supply of loose abrader producing dust emission only when sufficient momentum is available $u_{s*} > u_{*ts}H$ (energy-limited). This assumption is unrealistic in dust source regions when the soil surface is rough, crusted (physical, chemical or biological) or sealed, or there is no sediment available to transport caused by rock fragments (armouring) at the soil surface (Chappell et al. 2007; Chappell et al. 2005, 2006; Gillette et al. 2001; Sekiyama et al. 2023; Vos et al. 2020; Webb and Strong 2011). We circumvent these poorly constrained modelling assumptions following recent developments (Hennen et al. 2022; Hennen et al. 2023) by using a novel calculation which combines the sediment transport

magnitude (Eq. 1) with the frequency distribution of dust emission (Eq. 6) when sediment transport and dust emission occurred

$$Q_{DPS}(\omega) = c\frac{\rho_a}{g}u_{s*}^3\,P(DPS > 0). \quad \text{(Eq. 7)}$$

Dust emission flux (F for particles <10 μm or PM_{10}; kg m^{-2} s^{-1}) is calculated following the classical scheme (Marticorena and Bergametti 1995) as a function of soil clay content

$$F_{AEM}(\omega, d, w) = \sum_d A_f A_s M Q_{AEM} 10^{(13.4\,\%_{clay} - 6.0)} \text{ with } 0\% < clay\% < 20\%, \quad \text{(Eq. 8)}$$

$$F_{DPS}(\omega) = \sum_d A_f A_s M Q_{DPS} 10^{(13.4\,\%_{clay} - 6.0)} \text{ with } 0\% < clay\% < 20\%. \quad \text{(Eq. 9)}$$

We restricted clay% to a maximum value of 20% consistent with previous work (Marticorena and Bergametti 1995) which showed reasonable results when applied in a regional model, notably calibrated to dust optical depth (Woodward 2001). The Q which produces dust, is adjusted by the emitted dust fraction M for a given particle size fraction with diameter d which we calculated as $1<d<10$ μm following Zender *et al.* (2003) by using M=0.87. The dust emission of a pixel is masked out if the soil surface is bare but frozen which inhibits dust emission (A_f). The dust emission of a given pixel is removed in the presence of any snow coverage (A_s). Unlike existing dust emission models, the use of ω_{ns} to dynamically estimate u_{s*} removes the need for vegetation indices and fixed vegetation coefficients to determine effective aerodynamic roughness. Furthermore, because u_{s*} is spatially explicit, it is not necessary to apply preferential dust source masks to pre-condition dust emission i.e., increasing dust emission in areas perceived to have greater erodibility and reducing dust emission from regions perceived as contributing little dust.

The arising hypothesis is that since some dust cycle models were calibrated to dust in the atmosphere, it is very likely that such calibrations have misled their development and / or

reduced the predictability of dust events. Consequently, we use an alternative recently established (Chappell and Webb 2016; Chappell et al. 2018; Ziegler et al. 2020), physically-based parameterization of changing soil surface wind friction velocity u_{s*} (**Figure 1**) which enables a dynamic (non-static over time) MODIS albedo-based (500 m; daily) dust emission model (AEM). However, this AEM like many dust emission models, is poorly constrained by crude assumptions of the sediment entrainment threshold and sediment supply. Therefore, we use a novel, recently established approach (Hennen et al. 2022; Hennen et al. 2023) (*Hennen et al., under review RSE; Supplementary manuscript supplied*) which replaces the AEM frequency distributions with (half, see below) the DPS frequency distributions. We compared DPS frequency converted to dust emission (F_{DPS}) with AEM dust emission (F_{AEM}) determined separately. We used least squares linear regression to fit a logarithmic function to the relation between F_{AEM} and F_{DPS} to correct for the expected over-estimation in F_{AEM} due to the poorly constrained model assumptions about entrainment and sediment supply. We used half of the DPS data to produce the calibration function (F_{cal}). We reserved the other half of these data for validation. To identify the DPS data to remove for the validation dataset, the DPS data were stratified systematically across the data range. Half of the DPS data were then selected randomly within each stratum. The validation was then performed by plotting F_{cal} against itself but using the validation data. The square root of the mean squared error (RMSE) was used to judge the goodness of model fit.

2.4 Albedo-based dust emission model implementation

In the calculation of the albedo-based dust emission (AEM) we use the time-varying ECMWF ERA5-Land (hourly; 11 km) daily maximum wind speed (10 m height U_{10}; **Figure 2A**), and soil moisture *w* (Muñoz Sabater 2019) (0-5 cm; **Figure 2B**). To adjust from the 5 cm soil moisture to a 1 cm layer for the model, we assumed a uniform distribution and

multiplied *w* by 1/5. We used the latest, reliable, spatially varying layers of soil surface (0-5 cm) particle size mass fraction in % for clay (0-2 µm), silt (2-50 µm) and sand (50-2000 µm) and soil bulk density from SoilGrids (250 m horizontal resolution) (Hengl et al. 2017)(**Figure 2C**). The SoilGrids prediction error for soil texture was around 10% and the variance explained by the modelling of these properties was around 75% (Hengl et al. 2017). We limited clay to a maximum 20% consistent with other modelling (Woodward 2001). We emphasise for subsequent discussion below, that there are very few areas with <5% clay (which strongly influences dust emission; Eqs 8 & 9) in the majority of North Africa and parts of the Middle East (**Figure 2C; Table 1**).

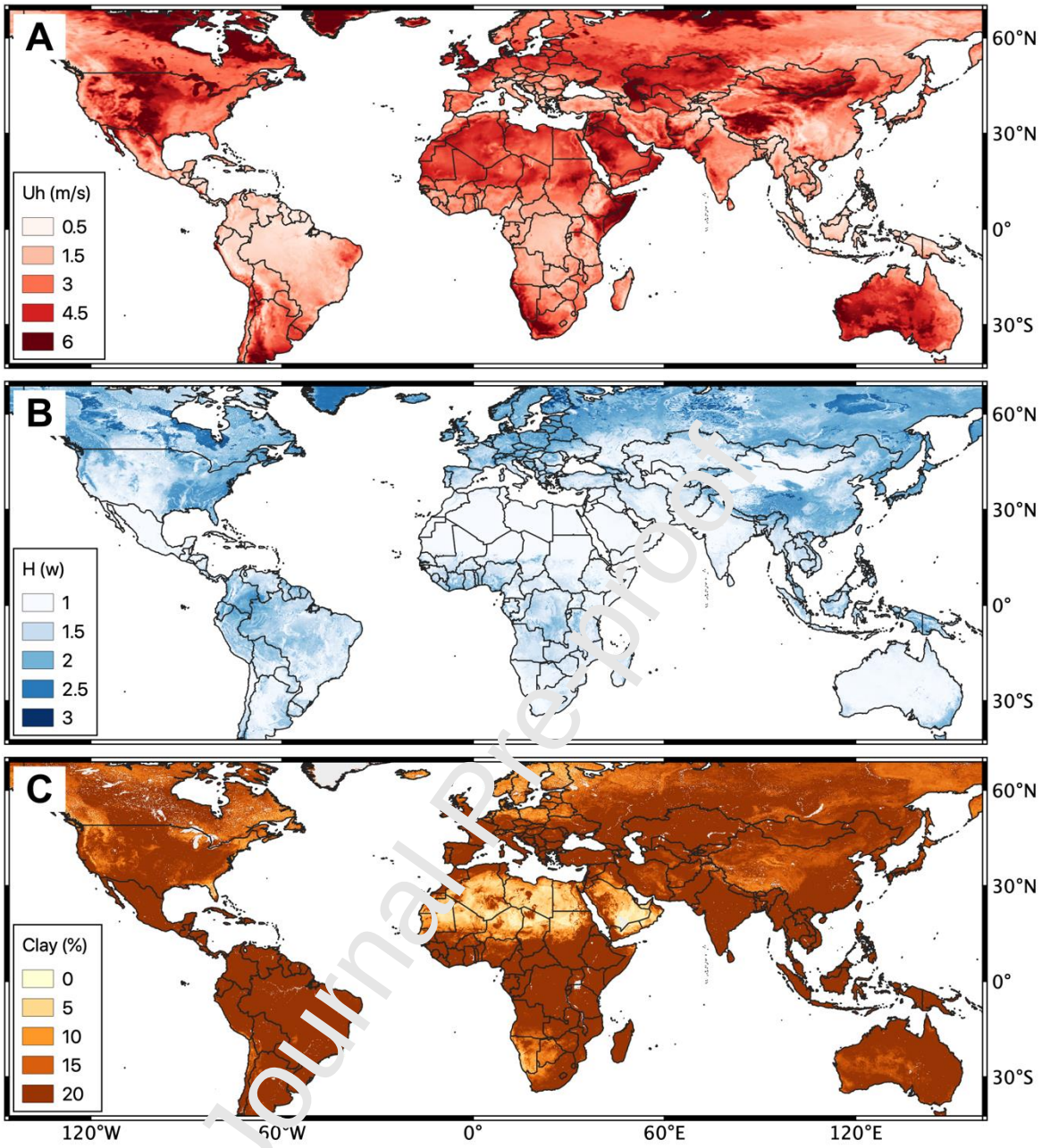

Figure 2. Examples of the data from the year 2020 where temporally varying, used in the dust emission modelling include the global distribution of daily 10 m height average wind speed (U_{10}; **A**), the average volumetric soil moisture function ($H(w)$; **B**; 5 cm of soil surface layer) and the mass fraction of clay (**C**; 0-2 µm; %). The U_h and $H(w)$ data were from the ECMWF ERA5-Land reanalysis data every hour at ~11 km resolution (Muñoz Sabater 2019). Static clay data (250 m pixels) were produced as part of SoilGrids (Hengl et al. 2017).

We estimated daily u_{s*}/U_h with the established albedo-based approach using MODIS band 1 MODIS (620-670 nm) for ω_n (Chappell and Webb 2016; Chappell et al. 2018; Chappell et al. 2019). To establish u_{s*} we multiplied daily u_{s*}/U_h by daily wind speed U_{10} for every pixel across Earth (**Figure 3B**). Intermediate valued winds (from the same ERA5-Land wind field model) occur across most of North Africa and the Middle East (Figure 2A). Consequently, the soil surface wind friction velocity (u_{s*}) which drives sediment transport and dust emission (Eqs 1 & 7) is consistently intermediate in value across most of North Africa (Figure 3). The largest values of u_{s*} occur in all other dryland dust producing regions (Figure 3B; Table 1). Above 'canopy' wind friction velocity (u_*) is, across Earth's land surface, larger than u_{s*} demonstrating the influence of roughness (Figure 3A).

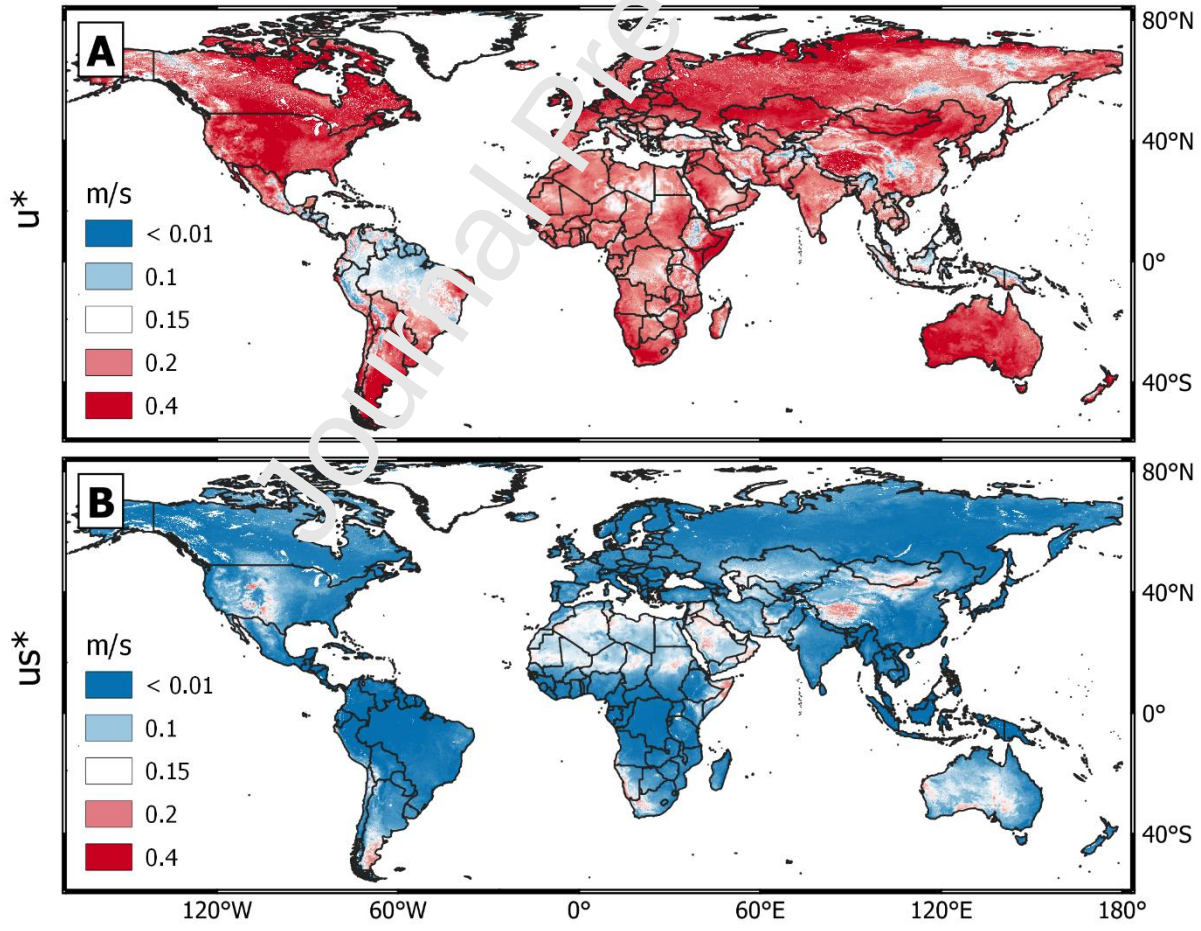

Figure 3. For the year 2020 the albedo-based wind friction velocity (u_*; **A**) is shown for comparison with the albedo-based soil surface wind friction velocity (u_{s*}; **B**) used in the albedo-based dust emission model (AEM). The AEM relates u_{s*} directly to normalised shadow (1-albedo) and uses MODIS albedo to enable spatio-temporal variation (every 500 m pixel, daily) with changing aerodynamic roughness and wind speed. Daily albedo data were obtained from the MODIS satellites (Schaaf and Wang 2015).

In a pixel, the presence of snow inhibits dust emission. We use the MODIS Normalised Difference Snow Index (NDSI; (Hall 2016)) available from Terra, daily at 500 m (MOD10A1 V6) to form a mask (A_s) where the occurrence of any snow causes sediment transport and dust emission to be removed at that pixel. Similarly, if the soil surface is bare but frozen it inhibits dust emission. We used the ERA5-Land soil temperature to produce a mask (A_f) with a conservative threshold of 273.15°K, above which sediment transport and dust emission can occur. The occurrence of standing water was similarly removed by using a MODIS land cover mask. No global calibration to aerosol optical depth or dust optical depth was applied.

2.5 Calculation of dust emission statistics

To summarise dust emissions patterns, we calculated statistics of grid-level dust emission stratified by land cover type and geographic region. The regions are similar to those used in previous studies (Ginoux et al. 2012). **Figure 4** shows the geographic distribution of the regions.

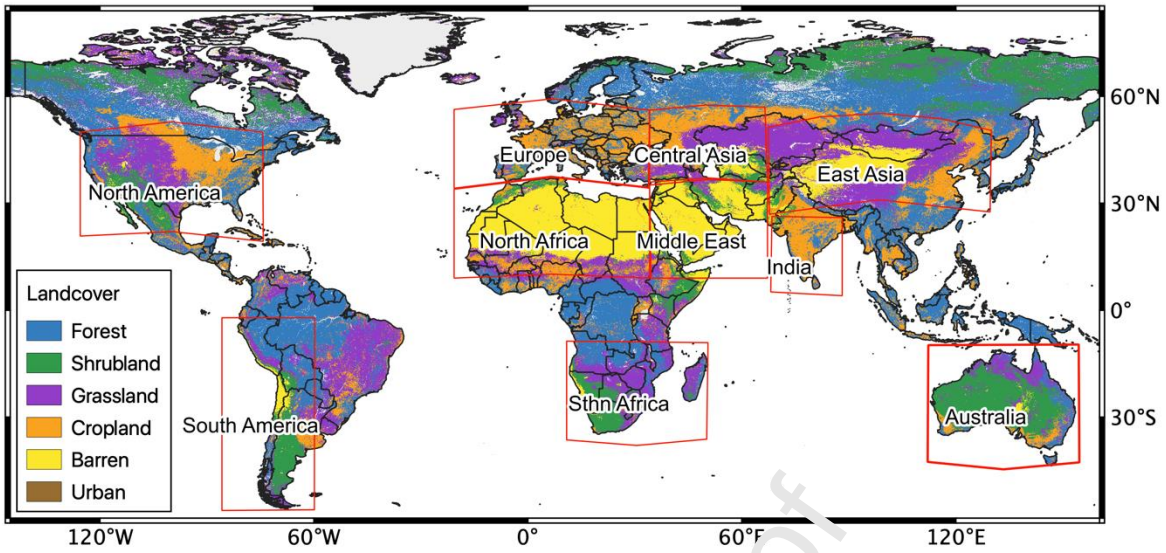

Figure 4. Geographic regions (red boxes) and land cover type from MODIS (MCD12Q1 collection 6) to aggregate modelled dust emission for summary statistics.

Dust emission statistics use land cover data by region (**Figure 4**). We used the IGBP classification. Although the land cover classification is recognised to have weaknesses particularly for cropland (Leroux et al. 2014), it is applied here globally and consistently to indicate the relative contributions rather than absolute amounts.

3. Results

3.1 Calibration and validation of modelled dust emission

We use all available global DPS data (**Figure 1**) to measure the frequency of dust emission events from Earth's major dust producing regions. For comparison, we use MODIS dust optical depth (DOD>0.2) frequency of occurrence and note a strong spatial correlation (R^2=0.85) between DOD and AERONET optical depth (Ginoux et al. 2012). The DOD frequency of dust is >100 days y^{-1} in all the dust producing regions (**Figure 1**). In contrast, the DPS frequency of dust is <100 days y^{-1} in North Africa and the Middle East and <10 dust days y^{-1} in all other dust producing regions (**Figure 1**). We compare our new collation of

DPS frequency data with DOD frequency data which reveals at this scale over time and space, there is very little global relation between the two datasets (**Figure 1 & 5A**). In other words, dust in the atmosphere has little-to-no direct association with the spatio-temporal variation of dust emission at source. To further elaborate our findings we have included a video of data layers (Appendix 2) which describe DOD occurrence, monthly between 2001-2020. Our finding is intuitively reasonable considering the nature of DPS sources which occur upwind of dust plumes (Kandakji et al. 2020) which enhances DOD downwind at large scales. This finding has far-reaching implications for i) our new calibration of a global dust emission model and ii) for global dust cycle models used in Earth System Models (ESMs) calibrated against DOD within a region and typically to DOD of North Africa (Huneeus et al. 2011). We explore these implications next.

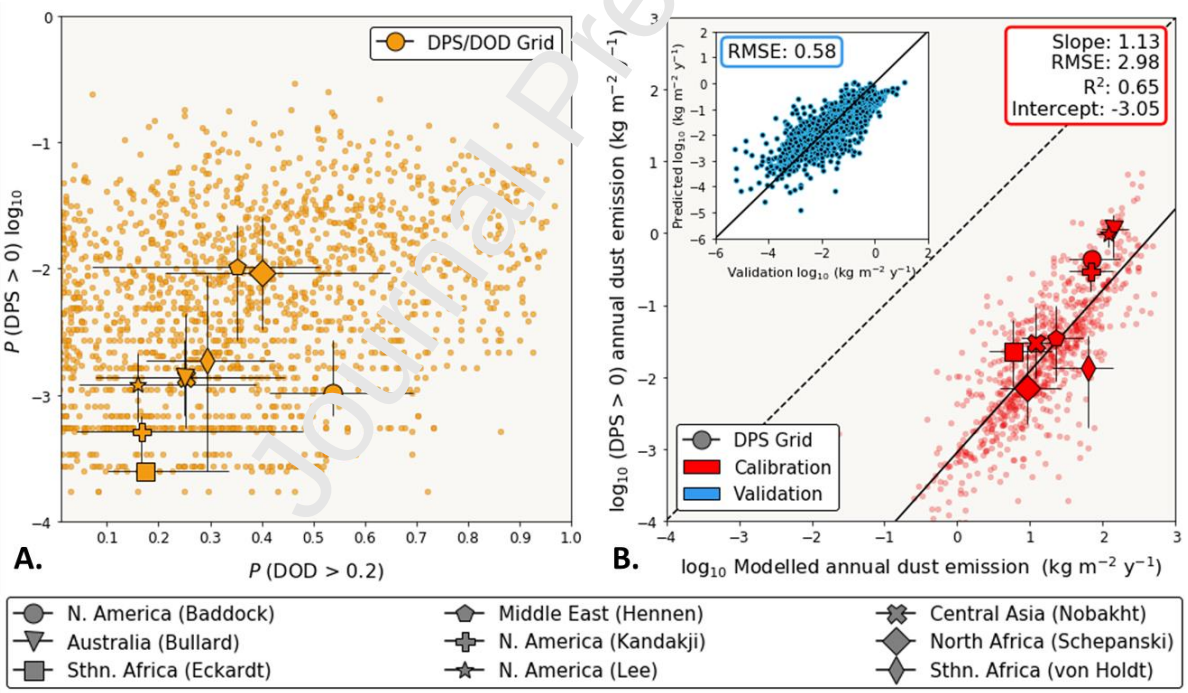

Figure 5. The poor relation is shown (**A**) between the frequency of satellite observations of dust emission point source data $\log_{10}$[P(DPS>0)] and the frequency of dust optical depth P(DOD>0.2) for the main dust source regions (orange symbols). In panel **B**, the magnitude of sediment transport and dust emission is calculated using the dust emission model driven by

albedo (AEM). The frequency distribution of sediment transport in the dust emission is provided by either F_{AEM} (Eq. 8; x-axis) or F_{DPS} data (Eq. 9; y-axis). Different symbols represent the dust source datasets / region median values, and their lines are the 25th and 75th percentiles of the variation. The inset plot shows the validation of the function fitted to the AEM data, by plotting F_{cal} against itself with DPS data unused in the calibration. The dashed line is the 1:1 line.

We compared DPS frequency converted to dust emission (F_{DPS}), with AEM dust emission (F_{AEM}) determined separately (**Figure 5B**). On average, the F_{AEM} over-estimated dust emission (RMSE= $10^{(2.98)}$ = 954 kg m^{-2} y^{-1}) relative to F_{DPS} data. This is expected, given the long-standing model assumptions of grain-scale threshold, static over time and fixed over space, and of an infinite supply of loose, erodible material everywhere across the Earth's land surface. We used least squares linear regression to fit a logarithmic function to F_{AEM} (R^2=0.65; P<<.001) and correct for the over-estimated model:

$$Log_{10}(F_{cal}) = 1.13Log_{10}(F_{AEM}) - 3.05. \quad \text{(Eq. 10)}$$

The validation of F_{cal} provided a reasonable (RMSE=$10^{(0.58)}$=3.80 kg m^{-2} y^{-1}) basis for global estimation of dust emission given the two orders of magnitude range in dust emission. This validation using DPS data is the first at the global scale and gives confidence that the calibrated dust emission (F_{cal}) represent the varying sources of dust emission where calibration samples may not: i) be available; ii) represent the region; iii) represent a long time period (in addition to other uncertainties related to data used e.g., MODIS revisit, wind speed scale). For example, East Asian (Gobi) and South American (mainly Argentina) dust sources are not represented in the existing DPS studies. North American, southern African, and Australian DPS measurements sample only a small part of the region and occur over only a small period within the modelling domain.

Figure 5B reveals that the uncalibrated AEM (F_{AEM}) is several orders of magnitude larger than F_{cal}, consistently between dust source regions. For the first time, we show that North Africa has the smallest, and Australia the largest followed closely by North America, dust emission per unit area (which describes emission efficiency). This validation is the first and currently best available estimate of dust emission model uncertainty and gives confidence that our findings are valid and representative of unsampled locations across the range of DPS data included.

3.2 Shifting predominant dust emission source regions and land covers.

We calculated the mean annual (2001-2020) calibrated dust emission (F_{cal}) every 500 m across Earth's land surface and displayed them seasonally (**Figure 6**). The results reveal multiple, globally predominant dust sources, shifting seasonally within and between hemispheres, not persistent North African dust emission primacy (**Figure 6**). North African F_{cal} is small and sparsely distributed across the region, caused by widespread intermediate soil surface wind friction velocity (u_{s*}; **Figure 1B**) and less than half the percentage clay of soils in other dust source regions (**Figure 2C; Eqs 8 & 9**). To further illustrate the spatial pattern of results, we have included a video of data layers (Appendix 2) which describes F_{cal} occurrences and DOD occurrences, monthly between 2001-2020. Evidently, this considerable regional difference in spatio-temporal dust emission magnitude and frequency between these results and those in the literature, has been hidden when models of dust emission are calibrated to atmospheric dust. We explain the cause of these differences in detail in section 4.

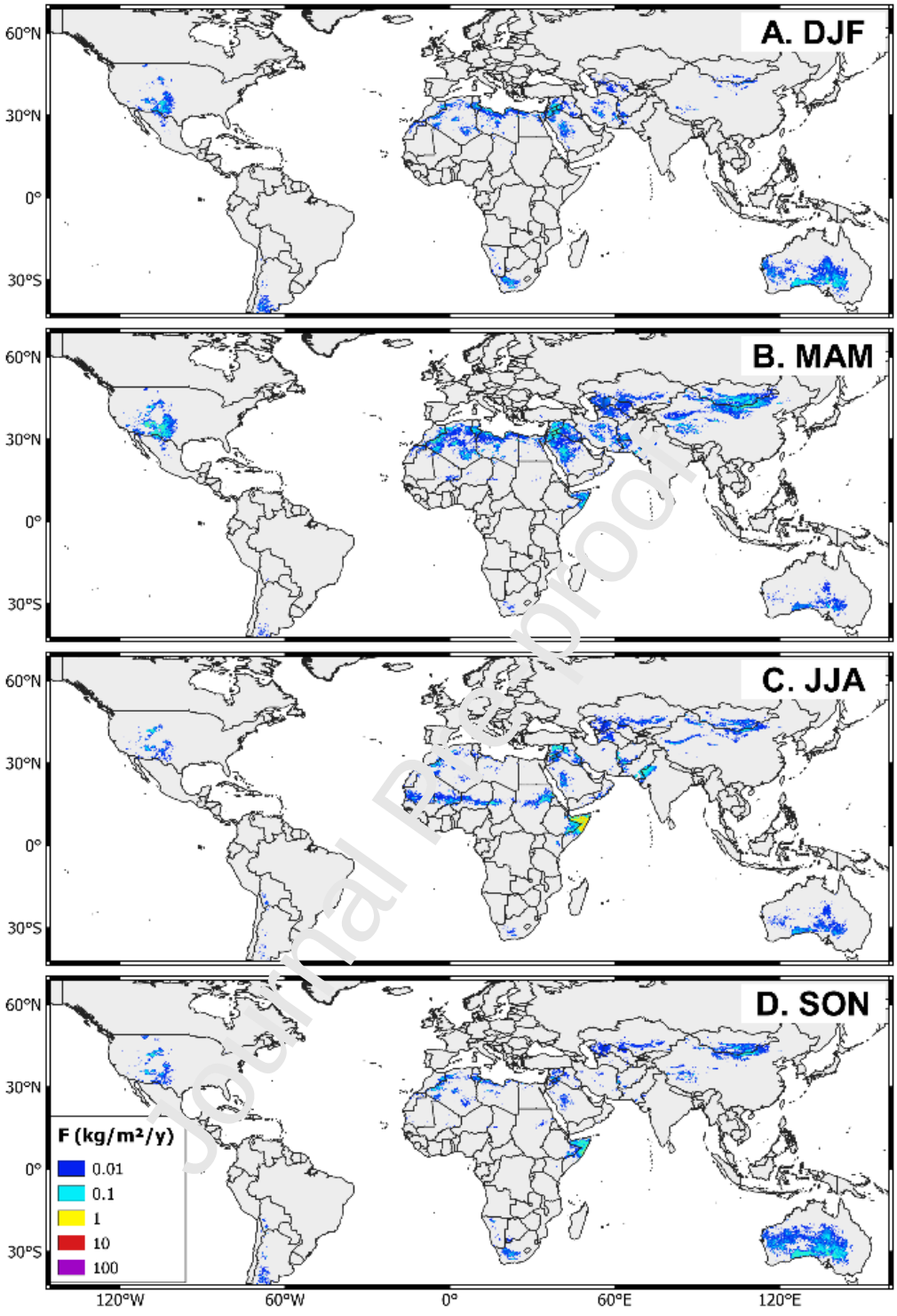

Figure 6. MODIS albedo mean annual (2001-2020) dust (PM_{10}) emission (kg m^{-2} y^{-1}) calibrated to DPS (F_{cal}; **A, B, C & D**), for the seasons of December-February (DJF), March-May (MAM), June-August (JJA) and September-November (SON). The dust emission is driven by ERA5-Land reanalysis wind fields and soil moisture, and SoilGrids clay content

(**Figure 2C**) (Hengl et al. 2017). Note the use of the logarithmic colour ramp to show the wide range of dust emission (not dust in the atmosphere) consistent with our uncertainty estimate of ±0.58($\log_{10}$) kg m^{-2} y^{-1}. The F_{cal} uses MODIS albedo data to represent the spatio-temporal variation in soil surface wind friction velocity (u_{s*}; **Figure 1B**).

To summarise the dust emission seasonality and understand the major global dust emission contributions by geographical region and land cover (**Figure 4**), we summed the F_{cal} monthly dust emission (**Figure 7**). The results confirm the patterns above, that North Africa is only briefly (Feb-Mar) seasonally predominant (**Figure 7A**). The Middle East, East Asia and Australia have seasonally larger dust emission than North Africa. However, North Africa is emitting dust consistently for more of the year than other regions. Between February to August monthly dust emission is largest from deserts (barren land), switching from North Africa and the Middle East (February-March) to East Asia (April-May) and then back to the Middle East (June-August; **Figure 7B**). Between April to May, there is a large contribution of dust emission from the grasslands of East Asia and North America, and a similar contribution from North American shrubland. During September-January, monthly dust emission is largest from Australian shrubland which switches dust source predominance to the Southern Hemisphere with far-reaching implications for revisions to ocean-atmosphere interactions in the past and the future.

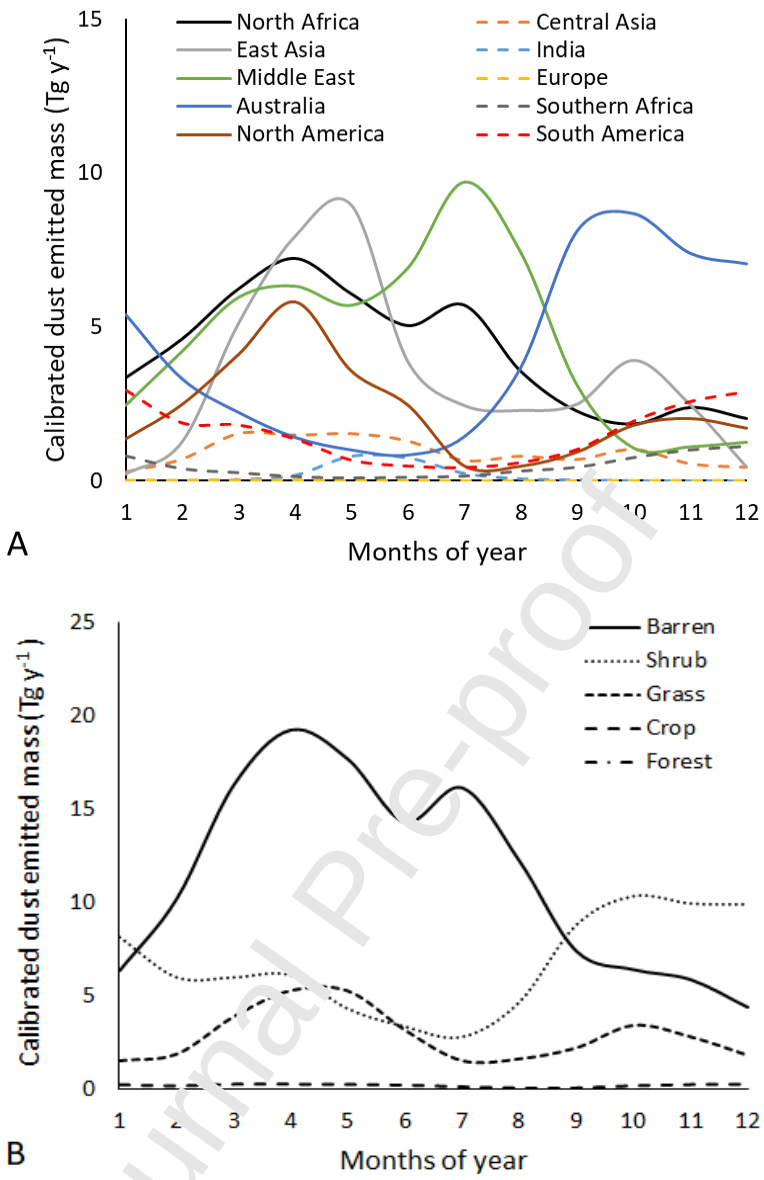

Figure 7. Total (2001-2020) monthly calibrated albedo-based dust emission seasonality (F_{cal}; Tg y^{-1}) stratified by global region (**A**) and by land cover (**B**). See **Figure 4** for definition of global regions and global land covers used in this study.

Averaging the dust emission over time and space, the largest F_{cal} dust emission source is from the land cover 'Barren Land' (roughly equivalent to deserts; 56.3%±15.9%) although shrublands (31.2%±8.6%) and grassland (11.9%±3.0%) are major contributors (**Table 2**). Dust emission from cropland makes no major contribution. Deserts dominating the Middle East produce the largest regional F_{cal} dust emission contribution (22.8%±6.4%). The average

annual (2001-2020) uncalibrated dust emission (F_{DPS}) is 12,972 Tg y^{-1}. The new F_{cal} estimate considerably reduces that mean to 29.1±14.9 Tg y^{-1}. That new mean F_{cal} is an order of magnitude smaller than the smallest dust cycle model estimates (514-4313 Tg y^{-1} up to 20 μm) (Huneeus et al. 2011) where dust emissions have been calibrated to dust in the atmosphere. Our new F_{cal} estimate is produced by a model that realistically represents the spatio-temporal variation in aerodynamic roughness, uses reliable clay content (cross-validated 72.5%) (Hengl et al. 2017) (**Figure 2C**) and the results are calibrated against all available DPS which includes most of the major global dust source areas (**Figure 1**).

Table 2. The average annual (2001-2020) dust (PM_{10}) emission calibrated albedo-based emission model (F_{cal}) using satellite observation of dust emission point source (DPS). The emissions account for daily varying emissive area and are stratified by global regions and global land covers (**Figure 4**).

Calibrated dust emission	**Shrub Land**	**Grass Land**	**Crop Land**	**Barren Land**	F_{cal} **Tg y^{-1}**	F_{cal} **%**
Australia	5.4±2.8	0.1±0.1	0.0±0.0	0.3±0.2	5.9±3.0	20.2±5.4
Central Asia	0.2±0.1	0.2±0.1	0.0±0.0	0.6±0.3	1.0±0.5	3.3±0.9
East Asia	0.1±0.0	1.3±0.7	0.0±0.0	3.1±1.6	4.5±2.3	15.4±4.2
Europe	0.0±0.0	0.0±0.0	0.0±0.0	0.0±0.0	0.0±0.0	0.0±0.0
India	0.1±0.1	0.0±0.0	0.0±0.0	0.0±0.0	0.2±0.1	0.5±0.1
Middle East	0.2±0.1	0.0±0.0	0.0±0.0	6.4±3.3	6.6±3.4	22.8±6.4
North Africa	0.1±0.1	0.1±0.1	0.0±0.0	5.7±2.9	6.0±3.1	20.5±5.7
North America	1.2±0.6	1.3±0.7	0.1±0.0	0.2±0.1	2.7±1.4	9.2±2.2
South America	1.5±0.8	0.2±0.2	0.0±0.0	0.0±0.0	1.9±1.0	6.4±1.7
Southern Africa	0.4±0.2	0.0±0.0	0.0±0.0	0.1±0.0	0.5±0.2	1.6±0.4
Total (Tg y^{-1})	9.1±4.7	3.5±1.8	0.2±0.1	16.4±8.4	29.1±14.9	
Total (%)	31.1±8.6	11.9±3.0	0.6±0.3	56.3±15.9		100.0

4. Discussion

4.1 Implications of calibrating dust cycle models to dust optical depth

More than two decades ago dust emission schemes were first developed (Joussaume 1990; Marticorena and Bergametti 1995; Shao et al. 1996). Since then, there has been no substantive change to the original dust emission model constraints that the i) entrainment

threshold at the grain-scale is fixed over space within substrate types, and static over time; ii) sediment supply for transport is infinite and available everywhere. Nevertheless, these schemes were rapidly adopted into large scale dust cycle models to form the dust emission (production) module of various ESMs. Dust emission is the beginning of the dust cycle and ultimately determines the net atmospheric dust concentration balanced by dust removal processes. An accurate representation of dust emission is key to an accurate estimate of dust feedbacks on e.g., radiation and cloud formation processes (Kok et al. 2023). Given these dust emission model assumptions, ESMs are well known to over-estimate dust in the atmosphere relative to dust optical depth observations (Zender et al. 2003a).

With the original focus of ESMs to represent all components of the dust cycle, it is common practice to evaluate the magnitude of modelled dust in the atmosphere by comparison with observed dust optical depth (DOD). ESMs are "…generally tuned to fit the observations in a given part of the world and often this tuning is done with observations from North Africa" (Huneeus et al. 2011)(p.7709). For example, the dust emission component of the dust emission model DEAD, required global tuning (T) down by several orders of magnitude (T=7 x 10^{-4}) to match DOD measurements (Zender et al. 2003a). However, DOD is a measure of the concentration of dust in a specific column of atmosphere at a given moment (Dubovik et al. 2000), not a direct measurement of dust emission magnitude and frequency which is inextricably bound together in the underpinning sediment transport equation (Lee and Tchakerian 1995; Wolman and Miller 1960). Our results confirm that at this scale in space and time, there is only a weak relation between satellite (MODIS / SEVIRI) observations of DPS dichotomous dust emission events and MODIS DOD frequency of occurrence (**Figure 5**). These results demonstrate that DOD frequency has little-to-no direct association with the spatio-temporal variation of dust emission frequency at source (Appendix 2. Figure A2 and A3). Regional studies have found long-term DOD

frequency of observation to be related to large-scale substrate types representing different dust emission potential (Baddock et al. 2016). The apparent contradiction between our results and those earlier DPS studies are very likely caused by responses occurring at different scales in time and space (Schumm and Lichty 1965). This topic is beyond the scope of this manuscript but worthy of investigation to explain the space, time and causality of dust emission.

4.2 Calibrating dust emission models to satellite observed dust emission point sources

Our uncalibrated dust emission (F_{DPS}) results relative to F_{cal}, were two orders of magnitude too large on average. This AEM over-estimation is much smaller than reported using dust emission models in dust cycle models (Zender et al. 2003a), due to our improved, direct estimation of the soil surface wind friction velocity. The over-estimation of uncalibrated dust emission models included in dust cycle models, particularly when tuning to North Africa, has important implications for ESMs. In this case, ESMs are very likely to simulate dust emission too frequently, with too little intensity in North Africa and with too little diversity from other dust mineralogical sources. For example, excluding different contributing atmospheric dust mineralogy from Asian grasslands and Australian shrublands is very likely to be important for Southern Hemisphere radiative forcing. Dust source masks (Ginoux et al. 2001) used to reduce preferentially regional or global dust source contributions have contributed to hiding the spatio-temporal distribution of dust emission as forewarned (Zender et al. 2003a).

Dust emission does not usually recur at the same location, and are rare (average 1.8%, ~7 days y^{-1}) even in North Africa and the Middle East, and indicative of large wind speed events (*Hennen et al., under review RSE; Supplementary manuscript supplied*). Our results show that relative to other regions with modelled dust emission, North Africa and the Middle

East have smaller soil surface wind friction velocity (u_{s*}; **Figure 3B; Table 1**) and less than half the clay content (**Figure 2C; Table 1**). Combined, these factors produce globally intermediate dust emission per unit area (cf. Eq. 9). In other words, North Africa and the Middle East have much reduced dust emission efficiency than other regions (e.g., North America and Australia) with more soil clay content and greater u_{s*}. However, across the vast dust producing region of North Africa, the large number of dust emissions over space and time, contribute to a large dust load and a frequently, very dusty atmosphere, which will not move quickly away from source due to smaller average wind speeds than other dust producing regions (**Figure 2A**). The implication is that North Africa has a large concentration of atmospheric dust in the boundary layer that is continually 'recycled' around the basins, suspended but not dispersed, or transported away from its generalised source and only occasionally exported across the Atlantic. Dust forming the background haze might be emitted only once, and kept aloft (e.g., by strong thermals) for long periods without moving much over space (Schepanski et al. 2012). The DOD over North Africa and the Middle East is frequently very large, consistent with these findings (e.g., DOD frequency Appendix 2. Figure A2).

4.3 Consistency of calibrated dust emission with regional dust climatology

Our AEM results show sporadic dust emission occurrences (<100 dust days y^{-1}) across North Africa and the Middle East consistent with the DPS to which they are calibrated. Our results are consistent with the patchy spatial distribution and the frequency of <135 days y^{-1} of dust plumes (within 2 km of the ground) identified independently from the Multiangle Imaging Spectroradiometer (MISR) motion vector product (Yu et al. 2018). In this region, our results are also consistent with the known weather systems, and particularly the seasonality of dust patterns (Caton Harrison et al. 2021; Cowie et al. 2014; Schepanski and Knippertz 2011).

These new insights to dust emission cannot be inferred from atmospheric DOD frequency which show persistently widespread North African atmospheric dust >100 days y^{-1} (Appendix 2. Figure A2 and A3).

Dust emission from the Bodélé Depression occurs in our model but is not large. This well-known dust source is typically omitted from large scale dust cycle models (Chappell et al. 2008; Tegen et al. 2002) because of its perhaps unique dust production. An expedition to the Bodélé Depression described a dust emission mechanism, where even light winds are accelerated over large (up to 50 m high) barchan dunes comprising quartz abrader and diatomite flakes which are abraded, emitting fine dust frequently into the atmosphere (Chappell et al. 2008; Warren et al. 2007). When low-level jets (LLJs) occur (Schepanski et al. 2009), this system enhances dust emission. However, this process of dune-accelerated abrading diatomite dust emission is not represented in any large-scale dust emission modelling and LLJs are not represented in large scale wind fields. Therefore, our dust emission model like all others of its kind, are unable to recognise the peculiar erodibility and erosivity conditions in the Bodélé Depression which produce frequent, large amounts of dust emission evident from ground measurements and DOD, over and downstream of, the Bodélé Depression (Chappell et al. 2008).

Dust emission contributions from Australia are larger than long-standing dust model estimates. Notably, global dust emission maps are often modified using dust source masks to reduce the dust emission from (Australian) sources to meet perceived expectations about dust source contributions (Albani et al. 2014; Evans et al. 2016). However, dust emission is well known to occur across a wide range of Australian land covers (Ekström et al. 2004; Strong et al. 2011) evident from long-term weather observations recording several different types of dust events to form the Australian dust storm index (O'Loingsigh et al. 2017; O'Loingsigh et

al. 2014). Furthermore, DOD frequency presented here shows extensive areas of dust in the atmosphere over Australia (Appendix 2; Figure A2).

4.4 Remaining uncertainties in calibrated dust emission modelling

We have provided the first estimates of global dust emission model uncertainty of ±3.8 kg m^{-2} y^{-1}, relative to regional dust emission observations. Our estimate and its uncertainty (29.1±14.9 Tg y^{-1}) are a benchmark of dust emission from regions and land covers (Table 2) for the ongoing development of dust emission models. The uncertainty is sufficiently small to enable our mapped differences in space and time (shown with a logarithmic scale; **Figure 6**) to be valid and therefore considered to be detectable. Considering the uncertainty estimate, there remain clear seasonal differences between the dust source regions which frequently produce small amounts of dust emission and when those regions which produce intermediate amounts of dust emission.

Our results suggest that the Horn of Africa is one of the largest sources of dust emission per unit area (indicating dust emission efficiency). We are cautious about this strong dust source, since preliminary inspections of optical satellite remote sensing from this region has not identified substantial dust emission. Whilst our model has evidently reduced uncertainty and bias, erroneous dust emission may remain, particularly where land surfaces are smooth but have no loose available sediment, or biogeochemical crusts seal the surface (Chappell et al. 2007; Chappell et al. 2005, 2006; Vos et al. 2020; Webb and Strong 2011). Other data layers on depth to bedrock and vegetation in the region indicate the widespread presence of soil, but it remains unclear whether loose erodible sediment is available. Whilst the dust modelling community is developing improved threshold and sediment supply model constraints, our dust emission model calibration against DPS data provides a solid foundation

for dust emission model implementation and operation in ESMs. Notwithstanding the improvements described here, dust emission modelling issues remain and require the following improvements (*Hennen et al., under review RSE; Supplementary manuscript supplied*):

- extend dust point source (DPS) studies to investigate a wider range of dust sources to evaluate the degree to which DPS data represent the magnitude and frequency of dust emissions associated with different atmospheric conditions
- develop an entrainment threshold which varies over space and time, and which is spatially area-weighted to overcome the incompatibility of the current grain (point) scale.
- apply consistently the same spatial scale for all area-based estimates, by linear scaling of the albedo data up to (e.g., 11 km) wind speed pixels before it is calibrated to the wind friction velocity.
- develop a parameterisation for sediment supply / availability changing over space which is spatially area-weighted and scales linearly for consistency with other model data.
- establish values for the above new model parameterisations by optimising against satellite observed dust emission (DPS) data.

4.5 Implications of calibrated dust emission modelling for dust cycle modelling

Our results indicate that dust emission models with currently poorly constrained threshold and sediment supply, before being included in ESMs must first be calibrated against DPS data and only then in the dust cycle model calibrated against DOD. While u_{*ts} remains poorly constrained, our new approach F_{DPS} (Eq. 9) and subsequent calibration F_{cal} (Eq. 10), enables a routine, single initial adjustment of the AEM. With its well-constrained magnitude of u_{s*} from calibrated wind tunnel measurements (Chappell and Webb 2016; Chappell et al.

2018), confirmed with recent field measurements (Ziegler et al. 2020), the F_{cal} provides maps of dust emission daily, every 500 m across Earth and which here and elsewhere (Hennen et al. 2022; Hennen et al. 2023) reveal temporal dynamics for spatially aggregated dust emission.

Our results indicate that calibrating dust cycle models to DOD, particularly to North African DOD alone, will over-estimate dust emission in that region and subsequently bias the magnitude of modelled dust emission in other regions. Avoiding this initial calibration of dust emission models against dust emission observations, will continue to prevent a clear direction in how to improve dust emission model fidelity and tackle the above recommendations. It is timely to note that uncertainties in CMIP6 models are larger than previous generations of models implying that modelled dust processes are becoming more uncertain as models develop (Zhao et al. 2022). Consequently, it is difficult to avoid the interpretation that calibrating dust cycle models to DOD has hidden the spatial patterns and magnitudes of dust emission shown here with implications for future dust-climate projections.

4.6 Implications of shifting global dust source predominance for dust-climate interactions

Our results reveal a previously hidden seasonal procession of dust emission in Earth's predominant dust sources (2001-2020) across a range of land covers including (in rank order) the Middle East and North African deserts, Australian shrublands, East Asian deserts and grasslands. Primacy is changed here because our dust emission estimates are not included in a dust cycle model and calibrated to (typically North African) DOD.

Seasonally shifting dust emission sources are entirely consistent with our understanding of climatology in global dust source regions (Cowie et al. 2014; Ekström et al. 2004; Knippertz and Todd 2012; Rivera Rivera et al. 2009; Shao and Dong 2006) and do not

contradict the prevailing view that North Africa has the greatest atmospheric dust concentration (Engelstaedter et al. 2006), long-established by dust optical depth measurements of dust in the atmosphere (Ginoux et al. 2001; Tegen et al. 2002; Woodward 2001). Our new, seasonally predominant dust emission sources, have quite different substrate types to one another and compared with North Africa. Variability in clay content maps has already established impacts for ESMs (Dai et al. 2019). The composition of clay minerals and iron oxides emitted to the atmosphere from our newly established dust emission sources (Middle Eastern desert, Australian shrublands and East Asian grassland and desert) will be quite different to those emitted with primacy from North Africa (Journet et al. 2014). The different mineralogy of the dust contributing sources combined with our dust emission mass reduced, by around two orders of magnitude (from 514–4313 Tg y^{-1} to 29.1±14.9 Tg y^{-1}), is very likely to change dust-climate interactions. Dust cycle models will need to account for the changed mineralogical contributions during the procession of these new spatially and seasonally varying dust emission sources.

The new major contributions of dust emission in the Southern Hemisphere, from Australia and to a lesser extent Argentina, during the relatively quiescent Northern Hemisphere (boreal) winter, will play a major and previously under-estimated role in Southern Hemisphere dust-climate interactions. Our results are expected to have far-reaching implications for ocean-atmosphere interactions (Crespi-Abril et al. 2018; Krishnamurthy et al. 2010; Paparazzo et al. 2018) including Southern Ocean productivity and the iron and quartz hypotheses (Boyd et al. 2007).

Our changed geographical ranking of dust emission sources will support necessary improvements in physically-based descriptions of dust residency and deposition modelling and the understanding of atmospheric dust transport (Adebiyi and Kok 2020) and dust-climate interactions (Kok et al. 2023). Finally, like all dust emission models, our results are

dependent on the input wind field. However, no one wind field best represents the characteristics of winds in all regions (Fan et al. 2021). Consequently, we make no claim that the results here are optimal, though they are 'internally' consistent.

5. Conclusion

Dust emission models currently have long-standing, unrealistic modelling assumptions including grain-scale threshold, static over time and fixed over space, and of an infinite supply of loose, erodible material everywhere across the Earth's land surface. These assumptions control the frequency distribution which influences the magnitude of geographical dust emission and causes considerable over-estimation in previous dust emission model estimates. To overcome the over-estimation due to these and other assumptions, previous dust emission models used in large scale dust cycle models have been calibrated against atmospheric dust (DOD and AERONET) typically to specific regions and commonly North Africa, which focuses the calibration solely on the magnitude of atmospheric dust in the region. Our results showed that at this spatio-temporal scale there is no relation between DOD frequency and satellite observed dust emission point sources (DPS) dichotomous data. Instead, our dust emission model was calibrated against DPS data by replacing the frequency distribution of the poorly constrained threshold and sediment model assumptions. The frequency distribution from DPS data improved the model constraint representing the magnitude and frequency of dust emission and provided for the first time a calibration uncertainty estimate of ±3.8 kg m^{-2} y^{-1}. Consequently, our results provided considerably smaller dust emission mass (29.1±14.9 Tg y^{-1}) and different spatio-temporal variation in dust emission to previous results, but consistent with the seasonality of the dust-producing regions. It is difficult to avoid the conclusion that these findings have been hidden

for more than two decades, since dust emission schemes were first developed, because dust cycle models have been calibrated to atmospheric dust concentrations.

Although able to reduce the magnitude and frequency of dust emission consistent with dust emission observations, our new calibration is unable to remove fundamentally incorrect sources where either there is no sediment lying loose on the surface or biogeochemical crusts have sealed the surface. Evidently, models of dust emission require new parameterisations to tackle these enduing model weaknesses. Notwithstanding this long-standing need for dust emission model improvement, the greatest potential of the AFM is its use of prognostic albedo with energy-based ESMs. Driving the dust cycle using albedo will enable its integration into land surface and climate energetic systems which will enable missing feedbacks and interactions between the dust cycle and the climate system, including land surface-atmosphere interactions e.g., land surface roughness changing aerodynamics, wind speeds, sediment transport and dust emission. The potential for more realistic modelling without additional complexity should reduce uncertainty of dust emission and improve climate change impacts. Furthermore, this new capability will enable carbon and nutrient fluxes to be coupled with sediment transport and dust emission modelling to demonstrate their impacts on carbon cycling, land degradation, food security and sustainable development (Chappell et al. 2016; Chappell et al. 2019; Webb et al. 2017).

6. Appendices

Appendix 1.

We used the entrainment threshold of a smooth surface u_{*ts} of a given d (mm) from Marticorena and Bergametti (1995):

$$u_{*ts}(d) = \begin{cases} \frac{0.129K}{(1.928Re^{0.092}-1)^{0.5}}, & 0.03<\text{Re}\leqslant 10 \text{ or Re}>10, \\ 0.129K(1-0.0858)e^{-0.0617(Re-10)} \end{cases} \quad \text{(Eq. A1)}$$

$$Re = aD^{x} + b; a = 1331cm^{-x}; b = 0.38; x = 1.56, \quad \text{(Eq. A2)}$$

$$K = \left(\frac{\rho_p g d}{\rho_a}\right)^{0.5}\left(1 + \frac{0.006}{\rho_p g d^{2.5}}\right)^{0.5}, \quad \text{(Eq. A3)}$$

includes p_a=1230 g m^3 fixed air density, p_p=2650 g m^3 fixed particle density, g=9.81 m s^{-2} acceleration due to gravity. The function developed by Shao and Lu (2000) is similar and both functions are shown in the Figure A1 to illustrate the dependency on soil particle size layer information which were based on clay, silt and sand soil texture from ISRIC (Hengl et al., 2017) and are fixed over time at 250 m pixel resolution. It is evident from Figure A1 that a threshold of around 0.2 m s^{-1} (20 cm s^{-1}) is associated with sediment transport and dust emission.

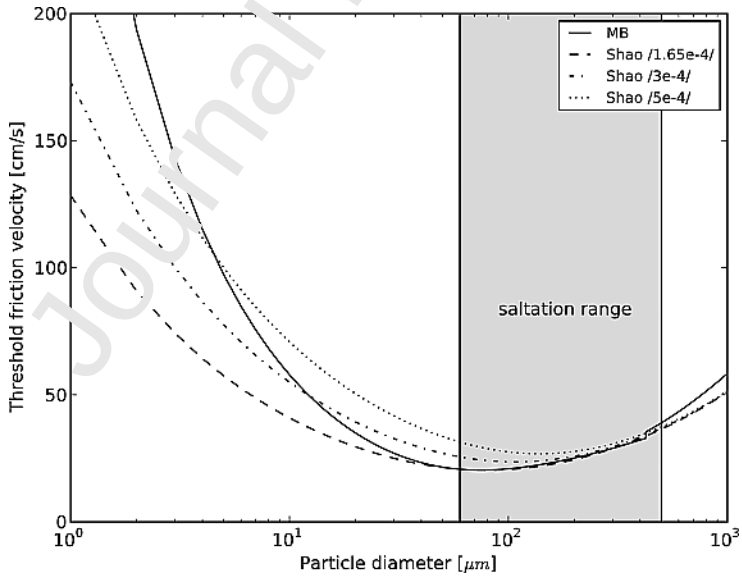

Figure A1. Threshold friction velocity over a smooth surface calculated with Marticorena and Bergametti (1995; MB) and Shao and Lu (2000; Shao) dust emission schemes (taken from Darmenova et al., 2009).

The dimensionless function *H* (Fecan et al., 1999) was developed using wind tunnel experiments to account for gravimetric surface soil moisture content *w* (kg^3 kg^{-3}) using the difference between the potential *w'* based on clay content and near surface *w*:

$$H(w) = \sqrt{1 + (1.21(w - w')^{0.68})} \quad \text{(Eq. A4)}$$

where

$$w' = 0.0014\%clay^2 + 0.17\%clay\,, \quad \text{(Eq. A5)}$$

and clay is the finest fraction (expressed as a percentage) of the soil and typically less than 2 µm.

Appendix 2.

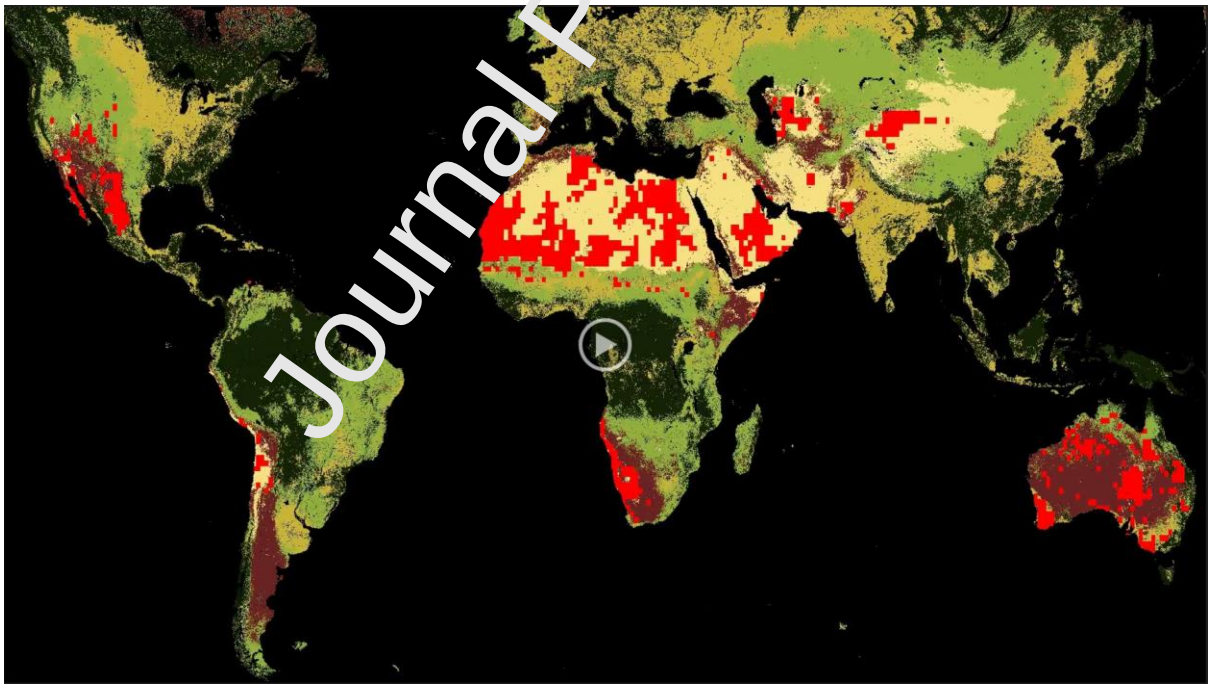

Figure A2. Animation video (Ctrl+click above image; 47 seconds; 5 frames per second) of monthly (one frame) average dust optical depth occurrence (DOD>0.2) between 2001-2020 displayed at 1-degree pixel resolution. MODIS land cover is used as the background.

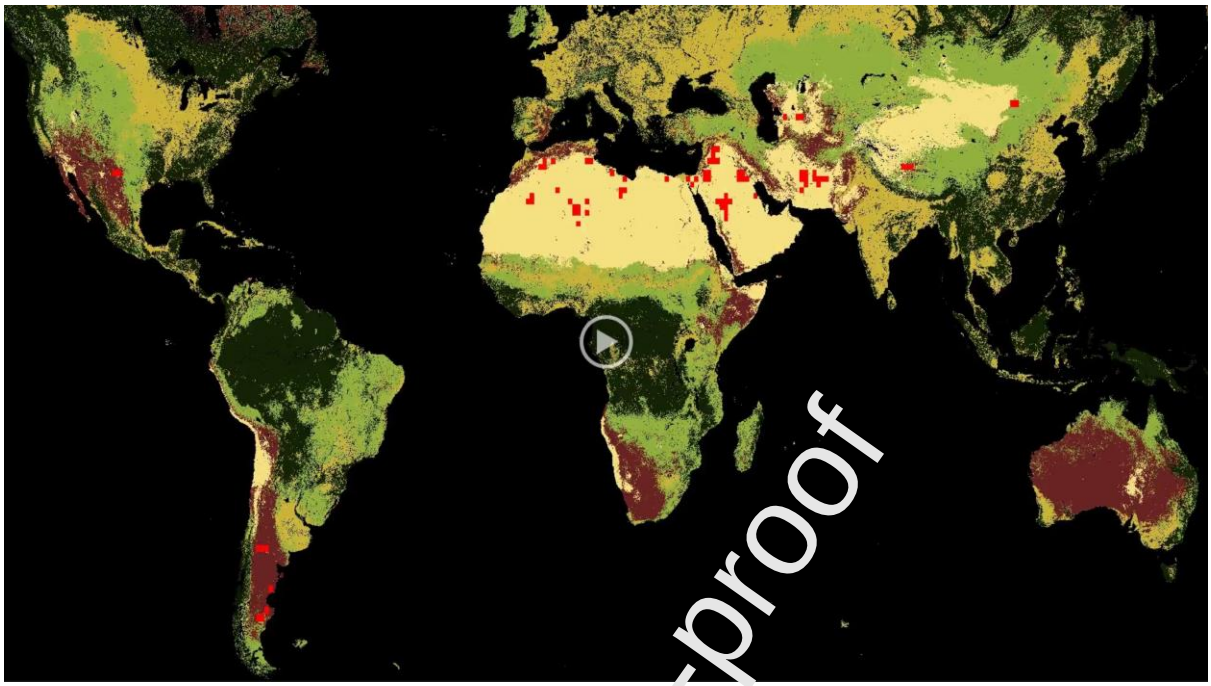

Figure A3. Animation video (Ctrl+click above image; 47 seconds; 5 frames per second) of monthly (one frame) average albedo-based dust emission model (AEM) calibrated to the dust emission point source (DPS) data (F_{cal}) occurrence (F_{cal}>0.01 kg m^{-2} y^{-1}) between 2001-2020 displayed at 1-degree pixel resolution. MODIS land cover is used as the background.

7. Acknowledgments

The first author is grateful to Google for access to and use of the Google Earth Engine (GEE) and support from Noel Gorelick and coding advice from GEE forum members. We thank the following people for their comments on earlier drafts of the manuscript: Beatrice Marticorena and Gilles Bergametti, LISA; Amato Evan, Scripps Institution of Oceanography; Stephanie Woodward and Malcolm Brooks, UK Met Office; Paul Ginoux, NOAA; Jasper Kok, UCLA; Natalie Mahowald, Cornell University; Ian Hall and Huw Davies, Cardiff University. We

thank the following for providing their dust point source data: Jo Bullard, Loughborough University, Kevin White and Maria Shahgedanova, Reading University. We also thank the following organisations for the use of their data: ECMWF, ERA5-Land data; NASA EOSDIS Land Processes Distributed Active Archive Center (LP DAAC), USGS/Earth Resources Observation and Science (EROS) Center, Sioux Falls, South Dakota; ISRIC SoilGrids. The work was produced whilst AC and NPW were funded by a joint grant from the US National Science Foundation (EAR-1853853) and the UK Natural Environmental Research Council (NE/T002263/1).

8. References

Adebiyi, A.A., & Kok, J.F. (2020). Climate models miss most of the coarse dust in the atmosphere. *Science Advances, 6*, eaaz9507

Baddock, M.C., Bullard, J.E., & Bryant, R.G. (2009). Dust source identification using MODIS: A comparison of techniques applied to the Lake Eyre Basin, Australia. *Remote Sensing of Environment, 113*, 1511-1528

Baddock, M.C., Gill, T.E., Bullard, J.E., Acosta, M.D., & Rivera Rivera, N.I. (2011). Geomorphology of the Chihuahuan Desert based on potential dust emissions. *Journal of Maps, 7*, 249-259

Banks, J.R., & Brindley, H.E. (2013). Evaluation of MSG-SEVIRI mineral dust retrieval products over North Africa and the Middle East. *Remote Sensing of Environment, 128*, 58-73

Banks, J.R., Hünerbein, A., Heinold, B., Brindley, H.E., Deneke, H., & Schepanski, K. (2019). The sensitivity of the colour of dust in MSG-SEVIRI Desert Dust infrared composite imagery to surface and atmospheric conditions. *Atmos. Chem. Phys., 19*, 6893-6911

Banks, J.R., Schepanski, K., Heinold, B., Hünerbein, A., & Brindley, H.E. (2018). The influence of dust optical properties on the colour of simulated MSG-SEVIRI Desert Dust infrared imagery. *Atmos. Chem. Phys., 18*, 9681-9703

Bergametti, G., Rajot, J.L., Pierre, C., Bouet, C., & Marticorena, B. (2016). How long does precipitation inhibit wind erosion in the Sahel? *Geophysical Research Letters, 43*, 6643-6649

Boyd, P.W., Jickells, T., Law, C.S., Blain, S., Boyle, E.A., Buesseler, K.O., Coale, K.H., Cullen, J.J., de Baar, H.J.W., Follows, M., Harvey, M., Lancelot, C., Levasseur, M., Owens, N.P.J., Pollard, R., Rivkin, R.B., Sarmiento, J., Schoemann, V., Smetacek, V., Takeda, S., Tsuda, A., Turner, S., & Watson, A.J. (2007). Mesoscale Iron Enrichment Experiments 1993-2005: Synthesis and Future Directions. *Science, 315*, 612

Bullard, J., Baddock, M., McTainsh, G., & Leys, J. (2008). Sub-basin scale dust source geomorphology detected using MODIS. *Geophysical Research Letters, 35*

Caton Harrison, T., Washington, R., & Engelstaedter, S. (2021). Satellite-Derived Characteristics of Saharan Cold Pool Outflows During Boreal Summer. *Journal of Geophysical Research: Atmospheres, 126*, e2020JD033387

Chappell, A., Strong, C., McTainsh, G., & Leys, J. (2007). Detecting induced in situ erodibility of a dust-producing playa in Australia using a bi-directional soil spectral reflectance model. *Remote Sensing of Environment, 106*, 508-524

Chappell, A., Van Pelt, S., Zobeck, T., & Dong, Z. (2010). Estimating aerodynamic resistance of rough surfaces using angular reflectance. *Remote Sensing of Environment, 114*, 1462-1470

Chappell, A., Warren, A., O'Donoghue, A., Robinson, A., Thomas, A., & Bristow, C. (2008). The implications for dust emission modeling of spatial and vertical variations in horizontal dust flux and

particle size in the Bodélé Depression, Northern Chad. *Journal of Geophysical Research: Atmospheres, 113*

Chappell, A., & Webb, N.P. (2016). Using albedo to reform wind erosion modelling, mapping and monitoring. *Aeolian Research, 23*, 63-78

Chappell, A., Webb, N.P., Guerschman, J.P., Thomas, D.T., Mata, G., Handcock, R.N., Leys, J.F., & Butler, H.J. (2018). Improving ground cover monitoring for wind erosion assessment using MODIS BRDF parameters. *Remote Sensing of Environment, 204*, 756-768

Chappell, A., Webb, N.P., Leys, J.F., Waters, C.M., Orgill, S., & Eyres, M.J. (2019). Minimising soil organic carbon erosion by wind is critical for land degradation neutrality. *Environmental Science & Policy, 93*, 43-52

Cowie, S.M., Knippertz, P., & Marsham, J.H. (2013). Are vegetation-related roughness changes the cause of the recent decrease in dust emission from the Sahel? *Geophysical Research Letters, 40*, 1868-1872

Cowie, S.M., Knippertz, P., & Marsham, J.H. (2014). A climatology of dust emission events from northern Africa using long-term surface observations. *Atmos. Chem. Phys., 14*, 8579-8597

Crespi-Abril, A.C., Soria, G., De Cian, A., & López-Moreno, C. (2018). Roaring forties: An analysis of a decadal series of data of dust in Northern Patagonia. *Atmospheric Environment, 177*, 111-119

Dai, Y., Shangguan, W., Wei, N., Xin, Q., Yuan, H., Zhang, S., Liu, S., Lu, X., Wang, D., & Yan, F. (2019). A review of the global soil property maps for Earth system models. *SOIL, 5*, 137-158

Darmenova, K., Sokolik, I.N., Shao, Y., Marticorena, B., & Bergametti, G. (2009). Development of a physically based dust emission module within the Weather Research and Forecasting (WRF) model:

Assessment of dust emission parameterizations and input parameters for source regions in Central and East Asia. *Journal of Geophysical Research: Atmospheres, 114*

Dubovik, O., Smirnov, A., Holben, B.N., King, M.D., Kaufman, Y.J., Eck, T.F., & Slutsker, I. (2000). Accuracy assessments of aerosol optical properties retrieved from Aerosol Robotic Network (AERONET) Sun and sky radiance measurements. *Journal of Geophysical Research: Atmospheres, 105*, 9791-9806

Eckardt, F.D., Bekiswa, S., Von Holdt, J.R., Jack, C., Kuhn, N.J., Mogane, F., Murray, J.E., Ndara, N., & Palmer, A.R. (2020). South Africa's agricultural dust sources and events from MSG SEVIRI. *Aeolian Research, 47*, 100637

Ekström, M., McTainsh, G.H., & Chappell, A. (2004). Australian dust storms: temporal trends and relationships with synoptic pressure distributions (1960–99). *International Journal of Climatology, 24*, 1581-1599

Engelstaedter, S., Tegen, I., & Washington, R. (2006). North African dust emissions and transport. *Earth-Science Reviews, 79*, 73-100

Evan, A.T., Flamant, C., Fiedler, S., & Doherty, O. (2014). An analysis of aeolian dust in climate models. *Geophysical Research Letters, 41*, 5996-6001

Fan, W., Liu, Y., Chappell, A., Dong, L., Xu, R., Ekström, M., Fu, T.-M., & Zeng, Z. (2021). Evaluation of Global Reanalysis Land Surface Wind Speed Trends to Support Wind Energy Development Using In Situ Observations. *Journal of Applied Meteorology and Climatology, 60*, 33-50

Favet, J., Lapanje, A., Giongo, A., Kennedy, S., Aung, Y.-Y., Cattaneo, A., Davis-Richardson, A.G., Brown, C.T., Kort, R., Brumsack, H.-J., Schnetger, B., Chappell, A., Kroijenga, J., Beck, A., Schwibbert, K., Mohamed, A.H., Kirchner, T., de Quadros, P.D., Triplett, E.W., Broughton, W.J., & Gorbushina,

A.A. (2013). Microbial hitchhikers on intercontinental dust: catching a lift in Chad. *The ISME Journal, 7*, 850-867

Fécan, F., Marticorena, B., & Bergametti, G. (1999). Parametrization of the increase of the aeolian erosion threshold wind friction velocity due to soil moisture for arid and semi-arid areas. *Ann. Geophys., 17*, 149-157

Ginoux, P., Chin, M., Tegen, I., Prospero, J.M., Holben, B., Dubovik, O., & Lin, S.-J. (2001). Sources and distributions of dust aerosols simulated with the GOCART model. *Journal of Geophysical Research: Atmospheres, 106*, 20255-20273

Ginoux, P., Prospero, J.M., Gill, T.E., Hsu, N.C., & Zhao, M. (2012). Global-scale attribution of anthropogenic and natural dust sources and their emission rates based on MODIS Deep Blue aerosol products. *Reviews of Geophysics, 50*

Hall (2016). MODIS/Terra Snow Cover Daily L3 Global 500m Grid. Version 6. Boulder, Colorado USA. *NASA National Snow and Ice Data Center Distributed Active Archive Center*

Hengl, T., Mendes de Jesus, J., Heuvelink, G.B.M., Ruiperez Gonzalez, M., Kilibarda, M., Blagotić, A., Shangguan, W., Wright, M.N., Geng, X., Bauer-Marschallinger, B., Guevara, M.A., Vargas, R., MacMillan, R.A., Batjes, N.H., Leenaars, J.G.B., Ribeiro, E., Wheeler, I., Mantel, S., & Kempen, B. (2017). SoilGrids250m: Global gridded soil information based on machine learning. *PLOS ONE, 12*, e0169748

Hennen, M., Chappell, A., Edwards, B.L., Faist, A.M., Kandakji, T., Baddock, M.C., Wheeler, B., Tyree, G., Treminio, R., & Webb, N.P. (2021). A North American dust emission climatology (2001–2020) calibrated to dust point sources from satellite observations. *Aeolian Research*, 100766

Hennen, M., Chappell, A., Edwards, B.L., Faist, A.M., Kandakji, T., Baddock, M.C., Wheeler, B., Tyree, G., Treminio, R., & Webb, N.P. (2022). A North American dust emission climatology (2001–2020) calibrated to dust point sources from satellite observations. *Aeolian Research, 54*, 100766

Hennen, M., Chappell, A., & Webb, N.P. (2023). Modelled direct causes of dust emission change (2001–2020) in southwestern USA and implications for management. *Aeolian Research, 60*, 100852

Hennen, M., White, K., & Shahgedanova, M. (2019). An Assessment of SEVIRI Imagery at Various Temporal Resolutions and the Effect on Accurate Dust Emission Mapping. *Remote Sensing, 11*, 918

Huneeus, N., Schulz, M., Balkanski, Y., Griesfeller, J., Prospero, J., Kinne, S., Bauer, S., Boucher, O., Chin, M., Dentener, F., Diehl, T., Easter, R., Fillmore, D., Ghan, S., Ginoux, P., Grini, A., Horowitz, L., Koch, D., Krol, M.C., Landing, W., Liu, X., Mahowald, N., Miller, R., Morcrette, J.J., Myhre, G., Penner, J., Perlwitz, J., Stier, P., Takemura, T., & Zender, C.S. (2011). Global dust model intercomparison in AeroCom phase I. *Atmos. Chem. Phys., 11*, 7781–7816

IPCC (2013). *Climate Change 2013: The Physical Science Basis. Contribution of Working Group I to the Fifth Assessment Report of the Intergovernmental Panel on Climate Change*. Cambridge, United Kingdom and New York, NY, USA: Cambridge University Press

Jacquemoud, S., Baret, F., & Hanocq, J.F. (1992). Modeling spectral and bidirectional soil reflectance. *Remote Sensing of Environment, 41*, 123-132

Journet, E., Balkanski, Y., & Harrison, S.P. (2014). A new data set of soil mineralogy for dust-cycle modeling. *Atmos. Chem. Phys., 14*, 3801-3816

Joussaume, S. (1990). Three-dimensional simulations of the atmospheric cycle of desert dust particles using a general circulation model. *Journal of Geophysical Research: Atmospheres, 95*, 1909-1941

Kandakji, T., Gill, T.E., & Lee, J.A. (2020). Identifying and characterizing dust point sources in the southwestern United States using remote sensing and GIS. *Geomorphology, 353*, 107019

Knippertz, P., & Todd, M.C. (2012). Mineral dust aerosols over the Sahara: Meteorological controls on emission and transport and implications for modeling. *Reviews of Geophysics, 50*

Kok, J.F., Storelvmo, T., Karydis, V.A., Adebiyi, A.A., Mahowald, N.M., Evan, A.T., He, C., & Leung, D.M. (2023). Mineral dust aerosol impacts on global climate and climate change. *Nature Reviews Earth & Environment*

Krishnamurthy, A., Moore, J.K., Mahowald, N., Luo, C., & Zender, C.S. (2010). Impacts of atmospheric nutrient inputs on marine biogeochemistry. *Journal of Geophysical Research: Biogeosciences, 115*

Lee, J.A., Baddock, M.C., Mbuh, M.J., & Gill, T.E. (2012). Geomorphic and land cover characteristics of aeolian dust sources in West Texas and eastern New Mexico, USA. *Aeolian Research, 3*, 459-466

Lee, J.A., & Tchakerian, V.P. (1995). Magnitude and Frequency of Blowing Dust on the Southern High Plains of the United States, 1947–1989. *Annals of the Association of American Geographers, 85*, 684-693

Leroux, L., Jolivot, A., Bégué, A., Seen, D.L., & Zoungrana, B. (2014). How Reliable is the MODIS Land Cover Product for Crop Mapping Sub-Saharan Agricultural Landscapes? *Remote Sensing, 6*, 8541-8564

Mahowald, N.M., Kloster, S., Engelstaedter, S., Moore, J.K., Mukhopadhyay, S., McConnell, J.R., Albani, S., Doney, S.C., Bhattacharya, A., Curran, M.A.J., Flanner, M.G., Hoffman, F.M., Lawrence, D.M., Lindsay, K., Mayewski, P.A., Neff, J., Rothenberg, D., Thomas, E., Thornton, P.E., & Zender, C.S. (2010). Observed 20th century desert dust variability: impact on climate and biogeochemistry. *Atmos. Chem. Phys., 10*, 10875-10893

Marshall, J.K. (1971). Drag measurements in roughness arrays of varying density and distribution. *Agricultural Meteorology, 8*, 269-292

Marticorena, B., & Bergametti, G. (1995). Modeling the atmospheric dust cycle: 1. Design of a soil-derived dust emission scheme. *Journal of Geophysical Research: Atmospheres, 100*, 16415-16430

Muñoz Sabater, J. (2019). ERA5-Land hourly data from 1981 to present. *Copernicus Climate Change Service (C3S) Climate Data Store (CDS)*

Nobakht, M., Shahgedanova, M., & White, K. (2021). New Inventory of Dust Emission Sources in Central Asia and Northwestern China Derived From MODIS Imagery Using Dust Enhancement Technique. *Journal of Geophysical Research: Atmospheres, 126*, e2020JD033382

O'Loingsigh, T., Chubb, T., Baddock, M., Kelly, T., Tapper, N.J., De Deckker, P., & McTainsh, G. (2017). Sources and pathways of dust during the Australian "Millennium Drought" decade. *Journal of Geophysical Research: Atmospheres, 122*, 1246-1260

O'Loingsigh, T., McTainsh, G.H., Tews, E.K., Strong, C.L., Leys, J.F., Shinkfield, P., & Tapper, N.J. (2014). The Dust Storm Index (DSI): A method for monitoring broadscale wind erosion using meteorological records. *Aeolian Research, 12*, 29-40

Paparazzo, F.E., Crespi-Abril, A.C., Gonçalves, R.J., Barbieri, E.S., Villalobos, L.L.G., Solís, M.E., & Soria, G. (2018). Patagonian Dust as a Source of Macronutrients in the Southwest Atlantic Ocean. *Oceanography, 31*, 33-39

Peters, D.P., Havstad, K.M., Archer, S.R., & Sala, O.E. (2015). Beyond desertification: new paradigms for dryland landscapes. *Frontiers in Ecology and the Environment, 13*, 4-12

Platnick, S. (2015). MODIS Atmosphere L3 Monthly Product. *NASA MODIS Adaptive Processing System, Goddard Space Flight Center*

Raupach, M.R. (1992). Drag and drag partition on rough surfaces. *Boundary-Layer Meteorology, 60*, 375-395

Rivera Rivera, N.I., Gill, T.E., Gebhart, K.A., Hand, J.L., Bleiweiss, M.P., & Fitzgerald, R.M. (2009). Wind modeling of Chihuahuan Desert dust outbreaks. *Atmospheric Environment, 43*, 347-354

Rodriguez-Caballero, E., Stanelle, T., Egerer, S., Cheng, Y., Su, H., Canton, Y., Belnap, J., Andreae, M.O., Tegen, I., Reick, C.H., Pöschl, U., & Weber, B. (2022). Global cycling and climate effects of aeolian dust controlled by biological soil crusts. *Nature Geoscience*

Schaaf, C., & Wang, Z. (2015). MCD43A3 MODIS/Terra+Aqua BRDF/Albedo Daily L3 Global - 500m V006 [Data set]. NASA EOSDIS Land Processes DAAC. Accessed 2020-03-18 from https://doi.org/10.5067/MODIS/MCD43A3.006

Schepanski, K., & Knippertz, P. (2011). Soudano-Saharan depressions and their importance for precipitation and dust: a new perspective on a classical synoptic concept. *Quarterly Journal of the Royal Meteorological Society, 137*, 1431-1445

Schepanski, K., Tegen, I., Laurent, B., Heinold, B., & Macke, A. (2007). A new Saharan dust source activation frequency map derived from MSG-SEVIRI IR-channels. *Geophysical Research Letters, 34*

Schepanski, K., Tegen, I., & Macke, A. (2012). Comparison of satellite based observations of Saharan dust source areas. *Remote Sensing of Environment, 123*, 90-97

Schepanski, K., Tegen, I., Todd, M.C., Heinold, B., Bönisch, G., Laurent, B., & Macke, A. (2009). Meteorological processes forcing Saharan dust emission inferred from MSG-SEVIRI observations of subdaily dust source activation and numerical models. *Journal of Geophysical Research: Atmospheres, 114*

Schlichting, H. (1936). Experimentelle Untersuchungen zum Rauhigkeitsproblem. *Ingenieur-Archiv, 7*, 1-34

Sekiyama, T.T., Kurosaki, Y., Kajino, M., Ishizuka, M., Buyantogtokh, B., Wu, J., & Maki, T. (2023). Improvement in Dust Storm Simulation by Considering Stone Coverage Effects for Stony Deserts in East Asia. *Journal of Geophysical Research: Atmospheres, 128*, e2022JD037295

Shao, Y., & Dong, C.H. (2006). A review on East Asian dust storm climate, modelling and monitoring. *Global and Planetary Change, 52*, 1-22

Shao, Y., Raupach, M., & Leys, J. (1996). A model for predicting aeolian sand drift and dust entrainment on scales from paddock to region. *Soil Research, 34*, 309-342

Shao, Y., Wyrwoll, K.-H., Chappell, A., Huang, J., Lin, Z., McTainsh, G.H., Mikami, M., Tanaka, T.Y., Wang, X., & Yoon, S. (2011). Dust cycle: An emerging core theme in Earth system science. *Aeolian Research, 2*, 181-204

Sinclair, S.N., & LeGrand, S.L. (2019). Reproducibility assessment and uncertainty quantification in subjective dust source mapping. *Aeolian Research, 40*, 42-52

Strong, C.L., Parsons, K., McTainsh, G.H., & Sheehan, A. (2011). Dust transporting wind systems in the lower Lake Eyre Basin, Australia: A preliminary study. *Aeolian Research, 2*, 205-214

Tegen, I., Harrison, S.P., Kohfeld, K., Prentice, I.C., Coe, M., & Heimann, M. (2002). Impact of vegetation and preferential source areas on global dust aerosol: Results from a model study. *Journal of Geophysical Research: Atmospheres, 107*, AAC 14-11-AAC 14-27

Tong, D.Q., Wang, J.X.L., Gill, T.E., Lei, H., & Wang, B. (2017). Intensified dust storm activity and Valley fever infection in the southwestern United States. *Geophysical Research Letters, 44*, 4304-4312

von Holdt, J.R., Eckardt, F.D., & Wiggs, G.F.S. (2017). Landsat identifies aeolian dust emission dynamics at the landform scale. *Remote Sensing of Environment, 198*, 229-243

Vos, H.C., Fister, W., Eckardt, F.D., Palmer, A.R., & Kuhn, N.J. (2020). Physical Crust Formation on Sandy Soils and Their Potential to Reduce Dust Emissions from Croplands. *Land, 9*, 503

Warren, A., Chappell, A., Todd, M.C., Bristow, C., Drake, N., Engelstaedter, S., Martins, V., M'Bainayel, S., & Washington, R. (2007). Dust-raising in the dustiest place on earth. *Geomorphology, 92*, 25-37

Webb, N.P., Chappell, A., LeGrand, S.L., Ziegler, N.P., & Edwards, B.L. (2020). A note on the use of drag partition in aeolian transport models. *Aeolian Research, 42*, 100560

Webb, N.P., Marshall, N.A., Stringer, L.C., Reed, M.S., Chappell, A., & Herrick, J.E. (2017). Land degradation and climate change: building climate resilience in agriculture. *Frontiers in Ecology and the Environment, 15*, 450-459

Webb, N.P., & Strong, C.L. (2011). Soil erodibility dynamics and its representation for wind erosion and dust emission models. *Aeolian Research, 3*, 165-179

Wolman, M.G., & Miller, J.P. (1960). Magnitude and Frequency of Forces in Geomorphic Processes. *The Journal of Geology, 68*, 54-74

Woodward, S. (2001). Modeling the atmospheric life cycle and radiative impact of mineral dust in the Hadley Centre climate model. *Journal of Geophysical Research: Atmospheres, 106*, 18155-18166

Xi, X., & Sokolik, I.N. (2015). Seasonal dynamics of threshold friction velocity and dust emission in Central Asia. *Journal of Geophysical Research: Atmospheres, 120*, 1536-1564

Yu, Y., Kalashnikova, O.V., Garay, M.J., Lee, H., & Notaro, M. (2018). Identification and Characterization of Dust Source Regions Across North Africa and the Middle East Using MISR Satellite Observations. *Geophysical Research Letters, 45*, 6690-6701

Zender, C.S., Bian, H., & Newman, D. (2003a). Mineral Dust Entrainment and Deposition (DEAD) model: Description and 1990s dust climatology. *Journal of Geophysical Research: Atmospheres, 108*

Zender, C.S., Newman, D., & Torres, O. (2003b). Spatial heterogeneity in aeolian erodibility: Uniform, topographic, geomorphic, and hydrologic hypotheses. *Journal of Geophysical Research: Atmospheres, 108*

Zhao, A., Ryder, C.L., & Wilcox, L.J. (2022). How well do the CMIP6 models simulate dust aerosols? *Atmos. Chem. Phys., 22*, 2095-2119

Ziegler, N.P., Webb, N.P., Chappell, A., & LeGrand, S.L. (2020). Scale Invariance of Albedo-Based Wind Friction Velocity. *Journal of Geophysical Research: Atmospheres, 125*, e2019JD031978

Author contributions

AC and NPW conceived the idea, AC coded the dust emission models in the Google Earth Engine, MH coded the satellite observed dust emission point source (DPS) analysis in Python. AC and NPW produced the first draft of the manuscript. All authors contributed to improving the manuscript prior to submission.

Declaration of interests

☒The authors declare that they have no known competing financial interests or personal relationships that could have appeared to influence the work reported in this paper.

☐The authors declare the following financial interests/personal relationships which may be considered as potential competing interests:

Graphical abstract

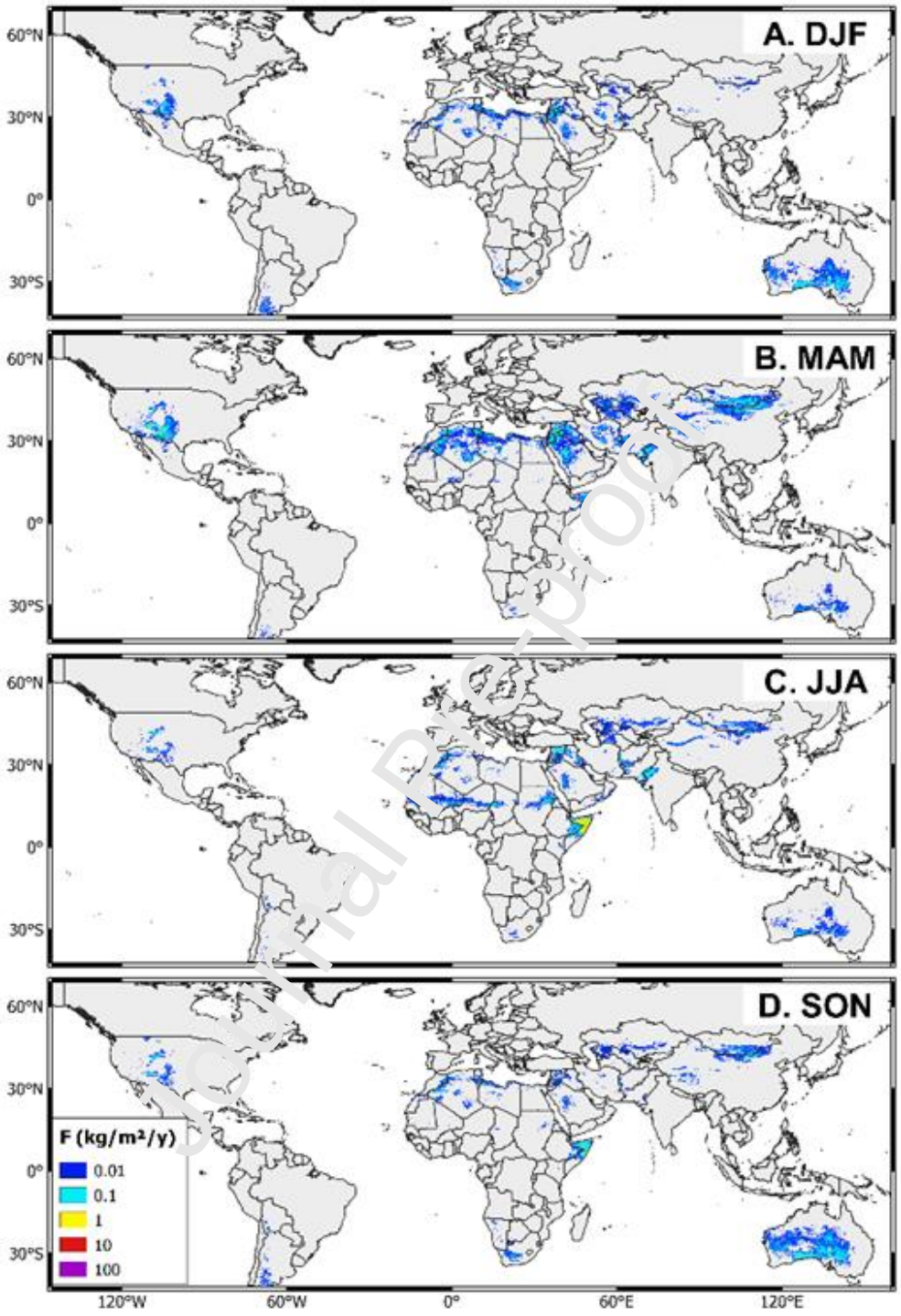

Mean annual (2001-2020) dust (PM_{10}) emission (kg m^{-2} y^{-1}) from the MODIS albedo-based model (AEM) calibrated to dust emission point sources (F_{cal}; **A, B, C & D**), showing dust sources shifting between hemispheres and seasonally for December-February (DJF), March-May (MAM), June-August (JJA) and September-November (SON). The AEM is driven by ERA5-Land reanalysis wind fields and soil moisture, and SoilGrids clay content. Note the use of a logarithmic colour ramp to show the wide range of dust emission (not dust in the atmosphere) consistent with our uncertainty estimate of ±0.58(log_{10}) kg m^{-2} y^{-1}.

Highlights

- Satellite-observed dust emissions (DPS) show little relation with dust optical depth
- Albedo-based dust emission model is calibrated and validated against global DPS data
- Global dust emissions shift seasonally within and between hemispheres
- Not persistent North African dust emission primacy interpreted from atmospheric dust
- Far-reaching implications for current and future dust-climate effects